ACADEMIC PRESS

Available online at www.sciencedirect.com

SCIENCE DIRECT®

Journal of Sound and Vibration 261 (2003) 247–276

JOURNAL OF SOUND AND VIBRATION

www.elsevier.com/locate/jsvi

2-D time-harmonic BEM for solids of general anisotropy with application to eigenvalue problems

M. Denda[a,*], C.Y. Wang[b], Y.K. Yong[c]

[a] *Department of Mechanical and Aerospace Engineering, Rutgers University, 98 Brett Road, Piscataway, NJ 08854-8058, USA*

[b] *Schlumberger-Doll Research, Old Quarry Road, Ridgefield, CT 06877, USA*

[c] *Civil and Environmental Engineering Department, Rutgers University, 623 Bowser Road, Piscataway, NJ 08854-8014, USA*

Received 18 October 2001; accepted 30 April 2002

Abstract

We present the direct formulation of the two-dimensional boundary element method (BEM) for time-harmonic dynamic problems in solids of general anisotropy. We split the fundamental solution, obtained by Radon transform, into static singular and dynamics regular parts. We evaluate the boundary integrals for the static singular part analytically and those for the dynamic regular part numerically over the unit circle.

We apply the developed BEM to eigenvalue analysis. We determine eigenvalues of full non-symmetric complex-valued matrices, depending non-linearly on the frequency, by first reducing them to the generalized linear eigenvalue problem and then applying the QZ algorithm. We test the performance of the QZ algorithm thoroughly in comparison with the FEM solution. The proposed BEM is not only a strong candidate to replace the FEM for industrial eigenvalue problems, but it is also applicable to a wider class of two-dimensional time-harmonic problems.

1. Introduction

We propose the 2-D time-harmonic dynamic boundary element method (BEM) and apply it to the eigenvalue analysis of general anisotropic solids. Wang et al. [1] have developed the FEM programs for the eigenvalue analysis of the time-harmonic problems for general piezoelectric (including anisotropic) solids; the program was applied successfully in the analysis of piezoelectric/anisotropic resonators. In the face of ever increasing device frequency, however,

*Corresponding author. Tel.: +1-732-445-4391; fax: +1-732-445-3124.

E-mail address: denda@jove.rutgers.edu (M. Denda).

0022-460X/03/$ - see front matter
doi:10.1016/S0022-460X(02)00957-4

the FEM is experiencing stiff computing requirements. While the FEM must discretize the whole domain, the BEM for the linear problem models only the boundary of the domain and has the potential of reducing the computational burden of the FEM drastically. This is true if the proper fundamental solution of the problem is used in the time-harmonic BEM. For isotropic solids Kitahara [2] have formulated the BEM based on the fundamental displacement and traction solutions for the time-harmonic plates and 2-D elasticity problems. For the general anisotropic solids, the fundamental solution of the time-harmonic problem was obtained by Norris [3] and Wang and Achenbach [4]. We adopt the fundamental solution by Wang and Achenbach [4] and formulate the 2-D direct BEM for time-harmonic dynamic problems of general anisotropic solids.

Due primarily to the unavailability of the time-harmonic fundamental solutions and to their complex form, use of much simpler static fundamental solution in the time-harmonic BEM has been attempted. This introduces the volume integral (or area integral in 2-D) in addition to the boundary integral. Nardini and Brebbia [5] has proposed the dual reciprocity boundary element method (DRBEM) to reduce volume integrals into boundary integrals. Majority of the DRBEM papers on eigenvalue analysis of time-harmonic dynamic problems have dealt with the Helmholtz equation [6]. In general, numerical results of the eigenvalue analysis by the DRBEM are satisfactory only for lower eigenvalues and the method becomes impractical for higher eigenvalues.

Wang and Achenbach [4,7] have shown that the fundamental solution can be split into singular and regular terms; the singular term coincides with the fundamental solution of the static problem and the additional dynamic contribution is provided by the regular term. Thus the time-harmonic BEM contains the static BEM; we adopt the direct formulation of the static BEM by Denda [8]. The regular dynamic term of the fundamental solution is expressed by line integrals over the unit circle. Use of this fundamental solution in the BEM leads to double integrals over the unit circle and over the boundary element. Exploiting the regularity of the dynamic term, we exchange the order of integration, perform the integration over the boundary element analytically leaving only the line integral over the unit circle for numerical evaluation. We perform the detailed error analysis for the numerical evaluation of the dynamic part to propose a reliable and accurate integration scheme.

Among a broad range of the BEM applications, we have selected the eigenvalue analysis. The resulting eigenvalue problems face with complex-valued, non-symmetric full matrices with elements depending non-linearly on the frequency. Kitahara [2] used the direct eigenvalue search to obtain the determinant value as a function of the frequency. We reduce this non-linear eigenvalue problem to the generalized linear eigenvalue problem, which is solved by the QZ algorithm accurately. The performance of the QZ algorithm is tested thoroughly, first for an anti-plane strain problem with the analytic solution, then for the generalized plane strain problem with the FEM solution. The proposed BEM implementation combined with the non-linear eigenvalue solver provides a reliable platform for the computation of eigenfrequencies for solids with general anisotropy. The use of the time-harmonic fundamental solution provides a clean boundary only formulation of the BEM without domain integrals. It is a strong candidate to replace the traditional dual reciprocity BEM (DRBEM) and FEM designed for the eigenvalue problems. More important, the proposed BEM is generally applicable to a wider class of two-dimensional time-harmonic problems not limited to the eigenvalue analysis.

2. Basic equations for time-harmonic problems

Consider the two-dimensional elastodynamic problem in the linear general anisotropic solid, where the field quantities depend only on the coordinates x_1 and x_2. The equations of motion in terms of the displacement $\tilde{u}_i$ and body force $\tilde{f}_i$ density components are given by

$$\{\Gamma_{ij}(\partial_1,\partial_2)-\rho\partial_t^2\delta_{ij}\}\tilde{u}_j(\mathbf{x},t)=-\tilde{f}_i(\mathbf{x},t), \tag{1}$$

where

$$\Gamma_{ij}(\partial_1,\partial_2)=c_{i\alpha j\beta}\partial_\alpha\partial_\beta, \tag{2}$$

$c_{i\alpha j\beta}$ are the stiffness tensor components, ρ is the mass density and $\mathbf{x}$ and t are the two-dimensional position vector and time, respectively. We adopt the convention that Roman and Greek subscripts range from 1 to 3 and 1 to 2, respectively; a repeated Roman or Greek index is summed over its full range. The derivative with respect to x_α of a function $\mathscr{F}$ is denoted either by $\mathscr{F}_{,\alpha}$ or $\partial_\alpha\mathscr{F}$, while its time derivative by $\partial_t\mathscr{F}$. Consider an infinite anisotropic solid subjected, at the origin and at time $t=-\infty$, to a time-harmonic line force in the x_k direction given by

$$\tilde{f}_j(\mathbf{x},t)=\delta_{jk}\delta(\mathbf{x})\mathrm{e}^{-\mathrm{i}\omega t}. \tag{3}$$

The resulting elastic displacement is in steady state motion and written as

$$\tilde{g}_{jk}(\mathbf{x},t)=g_{jk}(\mathbf{x},\omega)\mathrm{e}^{-\mathrm{i}\omega t}. \tag{4}$$

By substituting Eqs. (3) and (4) into Eq. (1) and omitting the time factor we get the equations

$$\{\Gamma_{ij}(\partial_1,\partial_2)+\rho\omega^2\delta_{ij}\}g_{jk}(\mathbf{x},\omega)=-\delta_{ik}\delta(\mathbf{x}), \tag{5}$$

whose solution, $g_{jk}(\mathbf{x},\omega)$, and the corresponding traction solution,

$$h_{jk}(\mathbf{x},\omega;\mathbf{v})=v_\alpha(\mathbf{x})c_{\alpha ji\beta}\frac{\partial g_{ik}(\mathbf{x},\omega)}{\partial x_\beta} \tag{6}$$

are called the fundamental displacement and traction solutions, where $\mathbf{v}$ is the unit normal to the segment where the traction is calculated. The Somigliana's identity gives the displacement in a body A in terms of these fundamental solutions and boundary traction (t_j) and displacement (u_j) by

$$u_k(\mathbf{x},\omega)=\int_{\partial A}t_j(\mathbf{y},\omega)g_{jk}(\mathbf{y}-\mathbf{x},\omega)\,\mathrm{d}l(\mathbf{y})-\int_{\partial A}u_j(\mathbf{y},\omega)h_{jk}(\mathbf{y}-\mathbf{x},\omega;\mathbf{v})\,\mathrm{d}l(\mathbf{y}). \tag{7}$$

This equation is the basis of the direct formulation of the boundary element method for time-harmonic dynamic problems for solids of general anisotropy.

3. Fundamental solutions

3.1. Fundamental solution by radon transform

Wang and Achenbach [4,7] have obtained the fundamental displacement solution using the Radon transform which, for an arbitrary function $\mathscr{F}(\mathbf{x})$, is defined as

$$\hat{\mathscr{F}}(s,\mathbf{n})=\int\mathscr{F}(\mathbf{x})\delta(s-\mathbf{n}\cdot\mathbf{x})\,\mathrm{d}\mathbf{x}. \tag{8}$$

This is an integration of $\mathscr{F}(\mathbf{x})$ along a line $\mathbf{n}\cdot\mathbf{x}=s$, defined by a unit vector $\mathbf{n}=(n_1,n_2)$ and a scalar s, in two dimensions. The inverse Radon transform is defined by

$$\mathscr{F}(\mathbf{x})=\int_{|\mathbf{n}|=1}\bar{\mathscr{F}}(\mathbf{n}\cdot\mathbf{x},\mathbf{n})\,\mathrm{d}\mathbf{n}, \tag{9}$$

where

$$\bar{\mathscr{F}}(s,\mathbf{n})=\frac{1}{4\pi^2}\int_{-\infty}^{\infty}\frac{\partial_\sigma\hat{\mathscr{F}}(\sigma,\mathbf{n})}{s-\sigma}\,\mathrm{d}\sigma \tag{10}$$

and the integral in Eq. (9) is a line integral over a unit circle. In summary, the displacement fundamental solution is given by a sum of the static singular part g^S_{jk} and the dynamic regular part g^R_{jk},

$$g_{jk}(\mathbf{x},\omega)=g^S_{jk}(\mathbf{x})+g^R_{jk}(\mathbf{x},\omega). \tag{11}$$

Key formulas in the derivation of the fundamental solution are:

(1) Radon transform of Eq. (5) that gives

$$\{\Gamma_{ij}(\mathbf{n})\partial_s^2+\rho\omega^2\delta_{ij}\}\hat{g}_{jk}=-\delta_{ik}\delta(s), \tag{12}$$

where

$$\Gamma_{ij}(\mathbf{n})=\Gamma_{ij}(n_1,n_2)=c_{i\alpha j\beta}n_\alpha n_\beta; \tag{13}$$

(2) eigenvalue λ_m and vector V_{im} for the symmetric positive-definite matrix $\Gamma_{ij}(\mathbf{n})$ defined by

$$\Gamma_{ij}(\mathbf{n})V_{jm}=\lambda_m V_{im}\quad(m=1,2,3;\ \text{no sum on } m); \tag{14}$$

(3) adjoint matrix

$$E^m_{jk}=\mathsf{adj}[\Gamma_{jk}(\mathbf{n})-\lambda_m\delta_{jk}]; \tag{15}$$

(4) the phase velocity c_m and wave number k_m,

$$c_m=\sqrt{\lambda_m/\rho},\quad k_m=\omega/c_m; \tag{16}$$

(5) adjoint and determinant of matrix $\Gamma_{jk}(1,\eta)$,

$$F_{jk}(\eta)=\mathsf{adj}[\Gamma_{jk}(1,\eta)],\quad D(\eta)=\mathsf{det}[\Gamma_{jk}(1,\eta)]. \tag{17}$$

3.1.1. Static singular part

The static singular part is given by

$$g^S_{jk}(\mathbf{x})=G^S_{jk}(\mathbf{x})+C_{jk} \tag{18}$$

with

$$G^S_{jk}(\mathbf{x})=\frac{1}{\pi}\Im\sum_{m=1}^{3}\frac{F_{jk}(\eta_m)}{\partial_\eta D(\eta_m)}\log(z_m) \tag{19}$$

and

$$C_{jk} = -\frac{1}{\pi}\Im\sum_{m=1}^{3}\frac{F_{jk}(\eta_m)}{\partial_\eta D(\eta_m)}\log(\eta_m + i), \tag{20}$$

where

$$z_m = x_1 + \eta_m x_2 \tag{21}$$

and η_m ($m = 1, 2, 3$ with $\Im(\eta_m) > 0$) are three distinct roots of the sixth order characteristic polynomial

$$D(\eta) = 0. \tag{22}$$

The symbol $\Im$ in Eqs. (19) and (20) indicates the imaginary part of a complex variable. Without loss of generality, we assume three distinct roots in this paper. The coincident roots can be made distinct by introducing a small perturbation in the stiffness coefficients. The term $g^S_{jk}(\mathbf{x})$ in Eq. (18) is the elastostatic fundamental solution obtained by Wang [9]; $G^S_{jk}(\mathbf{x})$ in Eq. (19) is equivalent to the static fundamental solution (37) by Denda [8]. The latter differs from $g^S_{jk}(\mathbf{x})$ by the constant term C_{jk}. These constants are inessential in the formulation of the elastostatic BEM, but they are required in Eq. (18) for the time-harmonic BEM.

3.1.2. Dynamic regular part

The dynamic regular part is given by

$$g^R_{jk}(\mathbf{x}, \omega) = \int_{|\mathbf{n}|=1} \bar{g}^R_{jk}(\mathbf{n}\cdot\mathbf{x}, \mathbf{n})\,\mathrm{d}\mathbf{n}, \tag{23}$$

where

$$\bar{g}^R_{jk}(\mathbf{n}\cdot\mathbf{x}, \mathbf{n}) = \frac{1}{8\pi^2}\sum_{m=1}^{3}\frac{1}{\rho c_m^2}\frac{E^m_{jk}}{E^m_{qq}}\phi^R(k_m|\mathbf{n}\cdot\mathbf{x}|) \tag{24}$$

with

$$\phi^R(k_m|\mathbf{n}\cdot\mathbf{x}|) = \phi(k_m|\mathbf{n}\cdot\mathbf{x}|) + 2\log|\mathbf{n}\cdot\mathbf{x}| \tag{25}$$

and

$$\phi(\zeta) = \mathrm{i}\pi e^{i\zeta} - 2[\cos(\zeta)\mathsf{ci}(\zeta) + \sin(\zeta)\mathsf{si}(\zeta)]. \tag{26}$$

Functions $\mathsf{ci}(\zeta)$ and $\mathsf{si}(\zeta)$ are the sine and cosine integral functions. Note that logarithmic function in Eq. (25) removes the singularity of the function $\phi(k_m|\mathbf{n}\cdot\mathbf{x}|)$ at the origin. Without loss of generality, we assume three distinct c_m in Eq. (24). When some of c_m coincide, they can be made distinct by introducing a small perturbation or can use special formulas derived by Wang and Achenbach [4,7].

The corresponding traction contribution of the dynamic regular part, obtained by substituting Eq. (23) into Eq. (6), is given by

$$h^R_{jk}(\mathbf{x}, \omega; \mathbf{v}) = \int_{|\mathbf{n}|=1} \bar{h}^R_{jk}(\mathbf{n}\cdot\mathbf{x}, \mathbf{n}; \mathbf{v})\,\mathrm{d}\mathbf{n}, \tag{27}$$

where

$$\bar{h}_{jk}^{R}(\mathbf{n}\cdot\mathbf{x},\mathbf{n};\mathbf{v}) = \frac{1}{8\pi^2}\,\mathrm{sign}(\mathbf{n}\cdot\mathbf{x})\sum_{m=1}^{3}\frac{1}{\rho c_m^2}\frac{E_{jk}^{*m}}{E_{qq}^{m}}\phi^{R'}(k_m|\mathbf{n}\cdot\mathbf{x}|) \tag{28}$$

with

$$E_{jk}^{*m} = \gamma_{jr}E_{rk}^{m}, \quad \gamma_{jr} = v_\alpha c_{\alpha jr\beta} n_\beta \tag{29}$$

and the prime attached to the function indicates the derivative with respect to its argument such as

$$\phi^{R'}(k_m|\mathbf{n}\cdot\mathbf{x}|) = k_m\phi'(k_m|\mathbf{n}\cdot\mathbf{x}|) + 2\log'(|\mathbf{n}\cdot\mathbf{x}|). \tag{30}$$

Repeated indices r and α and β in Eq. (29) should be summed over the ranges 1–3 and 1–2, respectively. In the evaluation of integrals (23) and (27) we consider only one half of the unit circle; the contribution from the other half is identical due to the two-fold symmetry of the integrands.

3.2. Fundamental static solution by Stroh–Lekhnitskii formalism

The static singular part of the BEM, guided by the physical interpretation of Somigliana's identity [8], uses the fundamental displacement solutions for the line force and the dislocation dipole. The Stroh–Lekhnitskii (SL) formalism [8] provides a framework to derive these fundamental solutions in terms of the **L** and **A** matrices defined by

$$\mathbf{L} = [\mathbf{l_1},\mathbf{l_2},\mathbf{l_3},] = \begin{bmatrix} -\eta_1 L_{21} & -\eta_2 L_{22} & -\eta_3 l_3 L_{33} \\ L_{21} & L_{22} & l_3 L_{33} \\ l_1 L_{21} & l_2 L_{22} & L_{33} \end{bmatrix} \tag{31}$$

and

$$\mathbf{A} = [\mathscr{A}_1\mathbf{l_1}, \mathscr{A}_2\mathbf{l_2}, \mathscr{A}_3\mathbf{l_3}] \tag{32}$$

with

$$\mathscr{A}_\mathbf{m} = \begin{bmatrix} s_{16} - s_{11}\eta_m, & s_{12}, & s_{14} - s_{15}\eta_m \\ \frac{s_{26}-s_{21}\eta_m}{\eta_m}, & \frac{s_{22}}{\eta_m}, & \frac{s_{24}-s_{25}\eta_m}{\eta_m} \\ s_{56} - s_{51}\eta_m, & s_{52}, & s_{54} - s_{55}\eta_m \end{bmatrix}. \tag{33}$$

The coefficients S_{MN} $(M,N = 1,2,4,5,6)$ are the reduced compliance coefficients and η_m $(m = 1,2,3$ with $\Im(\eta_m) > 0)$ are roots of the sixth order characteristic equation,

$$d^{(4)}(\eta)d^{(2)}(\eta) - d^{(3)}(\eta)d^{(3)}(\eta) = 0, \tag{34}$$

where

$$d^{(4)}(\eta) = \eta^4 S_{11} - 2\eta^3 S_{16} + \eta^2(2S_{12} + S_{66}) - 2\eta S_{26} + S_{22},$$

$$d^{(3)}(\eta) = \eta^3 S_{15} - \eta^2(S_{14} + S_{56}) + \eta(S_{25} + S_{46}) - S_{24},$$

$$d^{(2)}(\eta) = \eta^2 S_{55} - 2\eta S_{45} + S_{44}$$

and

$$l_\alpha = \frac{d^{(3)}(\eta_\alpha)}{d^{(2)}(\eta_\alpha)} \ (\alpha = 1, 2), \quad l_3 = \frac{d^{(3)}(\eta_3)}{d^{(4)}(\eta_3)}. \tag{35}$$

These matrices are normalized by the relation

$$2 \sum_{i=1}^{3} L_{im} A_{im} = 1 \quad (m = 1, 2, 3). \tag{36}$$

Note that the roots of the characteristic equations (22) and (34) are the same.

Consider a line force in x_k direction at the origin; the resulting displacement component in the x_j direction at $z = x_1 + \mathrm{i}x_2$ is given by

$$G^S_{jk}(z) = \Im \frac{1}{\pi} \sum_{m=1}^{3} A_{jm} A_{km} \ln(z_m), \tag{37}$$

where $z_m = x_1 + \eta_m x_2$ $(m = 1, 2, 3)$ is the generalized complex variable. A dislocation dipole is an infinitesimal segment $\mathrm{d}z = \mathrm{d}y_1 + \mathrm{i}\mathrm{d}y_2$ (of length $\mathrm{d}s$) over which a displacement jump is prescribed. Consider a dislocation dipole at the origin in x_k direction; the resulting displacement component in x_j direction at $z = x_1 + \mathrm{i}x_2$ is given by

$$G^{S(d)}_{jk}(z)\,\mathrm{d}s = -\Im \frac{1}{\pi} \sum_{m=1}^{3} A_{jm} L_{km} \frac{\mathrm{d}\xi_m}{z_m}, \tag{38}$$

where $\mathrm{d}\xi_m = \mathrm{d}y_1 + \eta_m \,\mathrm{d}y_2$. Eqs. (37) and (19) provide two alternative and equivalent expressions for the static displacement fundamental solution, while Eq. (38), without $\mathrm{d}s$, coincides with the minus of the traction fundamental solution of the line force.

3.3. Anti-plane strain: case study

3.3.1. Analytical and numerical solutions

The regular dynamic part of the fundamental displacement solution in anti-plane strain of the isotropic materials is given, from Eqs. (23) and (24), by

$$g^{R_N}_{33}(\mathbf{y}, \mathbf{x}, \omega) = \int_{|\mathbf{n}|=1} \bar{g}^R_{33}(\mathbf{n} \cdot (\mathbf{y} - \mathbf{x}), \mathbf{n})\,\mathrm{d}\mathbf{n} = \frac{1}{8\pi^2} \frac{1}{\mu} \int_{|\mathbf{n}|=1} \phi^R(k_2 |\mathbf{n} \cdot (\mathbf{y} - \mathbf{x})|)\,\mathrm{d}\mathbf{n}, \tag{39}$$

where $\phi^R(k_2|\mathbf{n} \cdot (\mathbf{y} - \mathbf{x})|)$ is defined by Eq. (25) and μ is the shear modulus. The wave number k_2 is given by $k_2 = \omega/c_2$ in terms of the shear wave speed, $c_2 = \sqrt{\mu/\rho}$, where ρ is the density. The corresponding analytical solution is given by

$$g^{R_A}_{33}(\mathbf{y}, \mathbf{x}, \omega) = \frac{1}{4\mu} \left[-\left\{ Y_0(\kappa_2) - \frac{2}{\pi} \ln \frac{r}{2} \right\} + \mathrm{i} \mathrm{J}_0(\kappa_2) \right], \tag{40}$$

where J_0 and Y_0 are the zero order Bessel and Neumann functions, respectively, and

$$\kappa_2 = k_2 r \tag{41}$$

is the product of the wave number and the distance $r = |\mathbf{y} - \mathbf{x}|$. Since solution (39) has the form essentially identical to that for the generalized plane strain, the results of its error analysis serve as guidelines for the error estimation of the generalized plane strain solution.

3.3.2. Numerical integration of dynamic part

3.3.2.1. Number of subdivision of the half-unit circle. The kernel function $\phi^R(k_2|\mathbf{n}\cdot(\mathbf{y}-\mathbf{x})|)$ in Eq. (39), defined by Eqs. (25) and (26), has the form

$$\phi^R(\zeta_2) = \mathrm{i}\pi e^{\mathrm{i}\zeta_2} - 2[\cos(\zeta_2)\mathrm{ci}(\zeta_2) + \sin(\zeta_2)\mathrm{si}(\zeta_2)] + 2\log\zeta, \tag{42}$$

which can be split into oscillatory and non-oscillatory parts as follows:

$$\begin{aligned}\phi^{Ros}(\zeta_2) &= \mathrm{i}\pi e^{\mathrm{i}\zeta_2} = -\pi\sin(\zeta_2) + \mathrm{i}\pi\cos(\zeta_2),\\ \phi^{Rno}(\zeta_2) &= -2[\cos(\zeta_2)\mathrm{ci}(\zeta_2) + \sin(\zeta_2)\mathrm{si}(\zeta_2)] + 2\log\zeta,\end{aligned} \tag{43}$$

where $\zeta = |\mathbf{n}\cdot(\mathbf{y}-\mathbf{x})| = r\cos\theta$, $\zeta_2 = k_2\zeta = k_2 r\cos\theta$, $r = |\mathbf{y}-\mathbf{x}|$ and θ is the angle between the position vector $\mathbf{y}-\mathbf{x}$ and the unit vector $\mathbf{n}$. Fig. 1 shows plots of (a) imaginary and (b) real oscillatory parts, (c) real non-oscillatory part and (d) total real part, respectively, for $\kappa_2 = 20$. As the magnitude of κ_2 increases the oscillation becomes increasingly intensive requiring increasingly smaller size of sub-intervals for numerical integration. We select the sizes of the sub-interval to match the minimum half-wavelength of the oscillatory parts (AB in Fig. 2) as given by

$$\Delta\theta_{min} = \frac{\pi}{2} - \arccos\frac{\pi}{\kappa_2}. \tag{44}$$

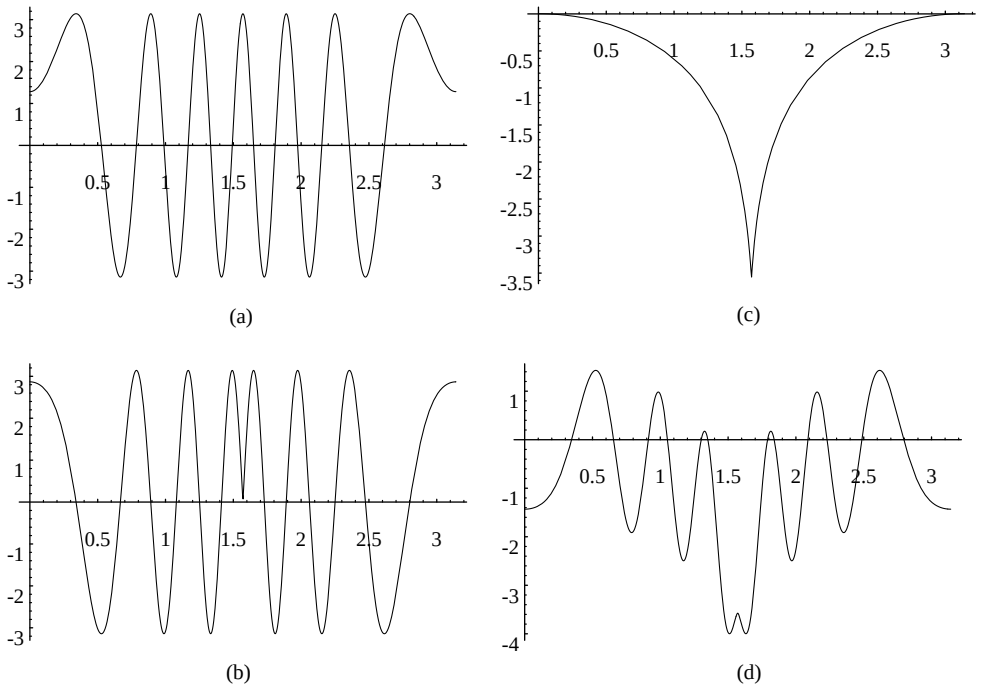

Fig. 1. Break up of the kernel function of Radon transformed fundamental solution: (a) imaginary part, (b) real oscillatory part, (c) real non-oscillatory part, (d) real part total.

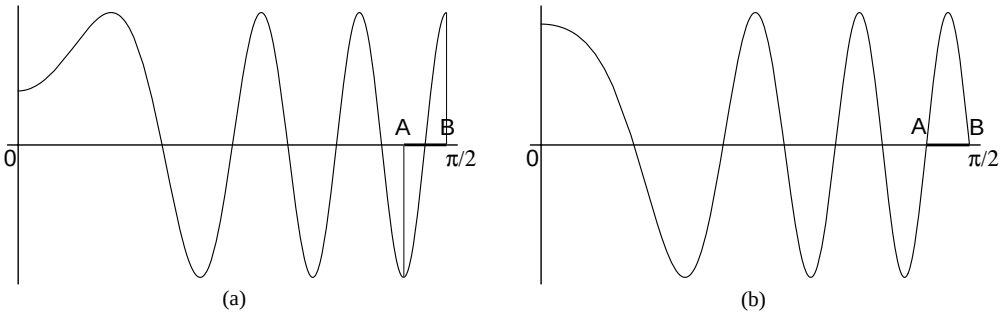

Fig. 2. Determination of the minimum sub-division size integration: (a) $\cos(\kappa_2 r\cos\theta)$, (b) $\sin(\kappa_2 r\cos\theta)$

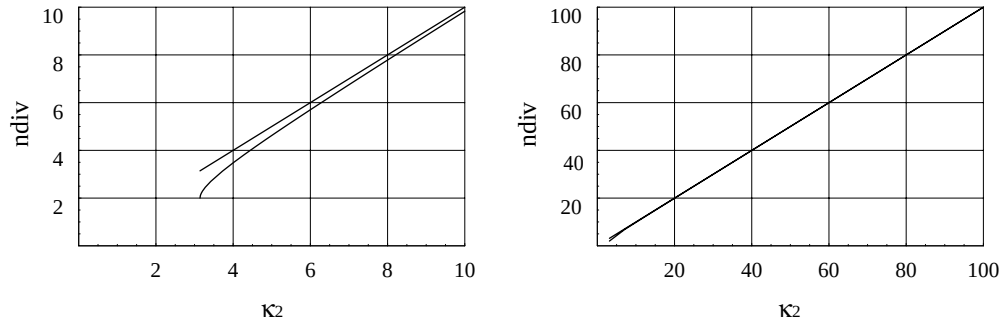

Fig. 3. Relation of the number of division per half-circle and κ_2.

This determines the number of sub-intervals along the half-circle,

$$n = \frac{1}{0.5 - (1/\pi)\arccos \pi/\kappa_2}, \tag{45}$$

which asymptotically approaches (Fig. 3) to

$$n = \kappa_2, \tag{46}$$

as κ_2 increases.

3.3.2.2. Number of Gauss quadrature points. As shown in Fig. 1, the kernel function $\phi^R(k_2|\mathbf{n}\cdot(\mathbf{y}-\mathbf{x})|)$ has a cusp at $\pi/2$ in the interval $(0,\pi)$ of integration; this cusp comes from the real non-oscillatory part (Fig. 1(c)). Integration must be split at this cusp to introduce two intervals, $(0,\pi/2)$ and $(\pi/2,\pi)$. After sub-dividing each interval uniformly we have refined it by further dividing the sub-interval closest to the cusp twice in a row. For this sub-division scheme of integration, the relative error of the real and imaginary parts is typically of the order of 10^{-8} if we use the Gauss quadrature points as recommended in Table 1 for various ranges of κ_2. The use of the same Gauss quadrature points for the uniform sub-division scheme of integration (i.e., no further sub-division near the cusp) results in the relative error of the order 10^{-7}.

Table 1
Optimum selection of the number of quadrature points p (for imaginary part) and q (for real part) of the Radon transformed fundamental solution

	Opt. no. of quad. pts.	
	p	q
$0 \leqslant \kappa_2 \leqslant 10$	5	7
$0 \leqslant \kappa_2 \leqslant 20$	4	6
$20 \leqslant \kappa_2 \leqslant 60$	4	5

4. Coefficients of boundary integral equations

4.1. Interpolation functions

We approximate the whole boundary by a collection of straight elements $\sum_\Gamma$; the straight element enables the analytical evaluation of the boundary integrals. Consider a boundary element Γ of length L with end (1, 2) and middle (3) nodes. The boundary displacement and traction are approximated by quadratic interpolation functions:

$$u_j(l) = \sum_{a=1}^{3} \psi_a(l) u_{ja}, \quad t_j(l) = \sum_{a=1}^{3} \psi_a(l) t_{ja}, \tag{47}$$

where $\psi_a(l)$ $(a = 1, 2, 3)$ are the quadratic shape functions of the arc length variable $0 \leqslant l \leqslant L$ given by

$$\psi_1(l) = \frac{2}{L^2}\left(l - \frac{L}{2}\right)(l - L), \quad \psi_2(l) = \frac{2}{L^2}\left(l - \frac{L}{2}\right) l, \quad \psi_3(l) = -\frac{4}{L^2} l(l - L) \tag{48}$$

and u_{ja} and t_{ja} are the nodal values of the interpolation functions u_j and t_j; the continuous elements are used. If we denote the dth derivative $(d = 0, 1, 2)$, with respect to l, of the interpolation functions by $u_j^{(d)}(l)$ and $t_j^{(d)}(l)$, then

$$u_j^{(d)}(l) = \sum_{a=1}^{3} \psi_a^{(d)}(l) u_{ja}, \quad t_j^{(d)}(l) = \sum_{a=1}^{3} \psi_a^{(d)}(l) t_{ja} \quad (d = 0, 1, 2), \tag{49}$$

where $\psi_a^{(d)}(l)$ is the dth derivative of the shape function with respect to l. As the time-harmonic fundamental solution is split into static singular and dynamic regular parts, so is the numerical implementation of the boundary elements. They are identified as the static singular boundary element (SSBE) and the dynamic regular boundary element (DRBE) implementations.

4.2. Static singular boundary element

There exist two alternative but equivalent formulas for the static fundamental displacement solution: Eq. (19) by the stiffness formulation and Eq. (37) by the compliance formulation. Wang et al. [10] used the fundamental displacement solution (19) and its traction solution for the implementation of the SSBE in their 2-D transient dynamic BEM. In contrast, Denda's static BEM [8] used the SSBE based on the fundamental displacement solution (37) and dislocation dipole solution (38). In both implementations, boundary integrals are evaluated analytically for the straight boundary element. In this paper we have adopted Denda's static BEM for the SSBE with due consideration of the contribution from the constant term C_{jk} defined by Eq. (20). Further details including closed-form boundary element formulas can be found in papers [8,11] by Denda.

4.3. Dynamic regular boundary element

According to Somigliana's identity (7) and the regular dynamic part of the fundamental solutions (23) and (27), the displacement contribution of a dynamic regular boundary element Γ is given by

$$u_k^R(\mathbf{x},\omega) = \int_\Gamma t_j(\mathbf{y},\omega)\left\{\int_{|\mathbf{n}|=1} \bar{g}_{jk}^R(\mathbf{n}\cdot(\mathbf{y}-\mathbf{x}),\mathbf{n})\,\mathrm{d}\mathbf{n}\right\}\mathrm{d}l(\mathbf{y}) - \int_\Gamma u_j(\mathbf{y},\omega)\left\{\int_{|\mathbf{n}|=1} \bar{h}_{jk}^R(\mathbf{n}\cdot(\mathbf{y}-\mathbf{x}),\mathbf{n};\mathbf{v})\,\mathrm{d}\mathbf{n}\right\}\mathrm{d}l(\mathbf{y}). \tag{50}$$

Due to the regularity of the integrands, $\bar{g}_{jk}^R(\mathbf{n}\cdot(\mathbf{y}-\mathbf{x}),\mathbf{n})$ and $\bar{h}_{jk}^R(\mathbf{n}\cdot(\mathbf{y}-\mathbf{x}),\mathbf{n};\mathbf{v})$, we can swap the order of the integration to get

$$u_k^R(\mathbf{x},\omega) = \int_{|\mathbf{n}|=1}\left\{\int_\Gamma t_j(\mathbf{y},\omega)\bar{g}_{jk}^R(\mathbf{n}\cdot(\mathbf{y}-\mathbf{x}),\mathbf{n})\,\mathrm{d}l(\mathbf{y})\right\}\mathrm{d}\mathbf{n} - \int_{|\mathbf{n}|=1}\left\{\int_\Gamma u_j(\mathbf{y},\omega)\bar{h}_{jk}^R(\mathbf{n}\cdot(\mathbf{y}-\mathbf{x}),\mathbf{n};\mathbf{v})\,\mathrm{d}l(\mathbf{y})\right\}\mathrm{d}\mathbf{n}. \tag{51}$$

The inner integrals in Eq. (51),

$$\bar{I}_k^{(\Gamma)}(\mathbf{x}\cdot\mathbf{n},\mathbf{n},\omega) = \int_\Gamma t_j(\mathbf{y},\omega)\bar{g}_{jk}^R(\mathbf{n}\cdot(\mathbf{y}-\mathbf{x}),\mathbf{n})\,\mathrm{d}l(\mathbf{y}),$$

$$\bar{J}_k^{(\Gamma)}(\mathbf{x}\cdot\mathbf{n},\mathbf{n},\omega) = \int_\Gamma u_j(\mathbf{y},\omega)\bar{h}_{jk}^R(\mathbf{n}\cdot(\mathbf{y}-\mathbf{x}),\mathbf{n};\mathbf{v})\,\mathrm{d}l(\mathbf{y}) \tag{52}$$

with interpolation (47) can be evaluated analytically as given by

$$\bar{I}_k^{(\Gamma)}(\mathbf{x}\cdot\mathbf{n},\mathbf{n},\omega) = \sum_{a=1}^{3}\sum_{j=1}^{3}\bar{\mathbf{I}}_{jka}(\mathbf{x}\cdot\mathbf{n},\mathbf{n},\omega)t_{ja},$$

$$\bar{J}_k^{(\Gamma)}(\mathbf{x}\cdot\mathbf{n},\mathbf{n},\omega) = \sum_{a=1}^{3}\sum_{j=1}^{3}\bar{\mathbf{J}}_{jka}(\mathbf{x}\cdot\mathbf{n},\mathbf{n},\omega)u_{ja} \tag{53}$$

with

$$\bar{\mathbf{I}}_{jka}(\mathbf{x}\cdot\mathbf{n},\mathbf{n},\omega)=\frac{1}{8\pi^2}\sum_{m=1}^{3}\frac{1}{\rho c_m^2}\frac{E_{jk}^m}{E_{qq}^m}\mathscr{I}_a^m(\mathbf{x}\cdot\mathbf{n},\mathbf{n},\omega),$$
$$\bar{\mathbf{J}}_{jka}(\mathbf{x}\cdot\mathbf{n},\mathbf{n},\omega)=\frac{1}{8\pi^2}\sum_{m=1}^{3}\frac{1}{\rho c_m^2}\frac{E_{jk}^{*m}}{E_{qq}^m}\mathscr{J}_a^m(\mathbf{x}\cdot\mathbf{n},\mathbf{n},\omega) \tag{54}$$

and

$$\mathscr{I}_a^m(\mathbf{x}\cdot\mathbf{n},\mathbf{n},\omega)=-\sum_{d=1}^{3}\left(\frac{-1}{e_\alpha n_\alpha}\right)^d\left[\psi_a^{(d-1)}(l)\left\{\frac{\phi^{[d]}(\zeta_m)}{(k_m)^d}+2\ln^{[d]}(\zeta)\right\}\right]_{l=0}^{l=L},$$
$$\mathscr{J}_a^m(\mathbf{x}\cdot\mathbf{n},\mathbf{n},\omega)=-\sum_{d=1}^{3}\left(\frac{-1}{e_\alpha n_\alpha}\right)^d\left[\psi_a^{(d-1)}(l)\left\{\frac{\phi^{[d-1]}(\zeta_m)}{(k_m)^d}+2\ln^{[d-1]}(\zeta)\right\}\right]_{l=0}^{l=L}. \tag{55}$$

Here $\phi^{[d]}(\zeta_m)$ and $\ln^{[d]}(\zeta)$ are the dth integrals of $\phi(\zeta_m)$ and $\ln(\zeta)$ given by

$$\phi^{[0]}(\zeta_m)=\mathrm{i}\pi e^{\mathrm{i}\zeta_m}-2[\cos(\zeta_m)\mathrm{ci}(\zeta_m)+\sin(\zeta_m)\mathrm{si}(\zeta_m)],$$
$$\phi^{[1]}(\zeta_m)=\pi e^{\mathrm{i}\zeta_m}-2[\sin(\zeta_m)\mathrm{ci}(\zeta_m)-\cos(\zeta_m)\mathrm{si}(\zeta_m)],$$
$$\phi^{[2]}(\zeta_m)=-\mathrm{i}\pi e^{\mathrm{i}\zeta_m}+2[\cos(\zeta_m)\mathrm{ci}(\zeta_m)+\sin(\zeta_m)\mathrm{si}(\zeta_m)]-2\ln|\zeta_m|,$$
$$\phi^{[3]}(\zeta_m)=-\pi e^{\mathrm{i}\zeta_m}+2[\sin(\zeta_m)\mathrm{ci}(\zeta_m)-\cos(\zeta_m)\mathrm{si}(\zeta_m)]-2\zeta_m[\ln|\zeta_m|-1] \tag{56}$$

and

$$\ln^{[d]}(\zeta)=\frac{\zeta^d}{d!}\left\{\ln|\zeta|-\sum_{j=1}^{d}\frac{1}{j}\right\}\quad(d\geqslant 0), \tag{57}$$

in terms of the arguments,

$$\zeta_m=k_m\zeta,\quad \zeta=n_\beta(y_\beta-x_\beta)=n_\beta\{(y_\beta|_{l=0}+le_\beta)-x_\beta\}, \tag{58}$$

where $y_\beta|_{l=0}$ is the initial point and e_β is the unit vector along the boundary element Γ. Notice that no absolute value is taken for the arguments ζ_m and ζ except for terms $\ln|\zeta_m|$ and $\ln|\zeta|$. The analytical evaluation of integrals (52) in Eq. (51) gives the single integral representation

$$u_k^R(\mathbf{x},\omega)=\int_{|\mathbf{n}|=1}\bar{I}_k^{(\Gamma)}(\mathbf{x}\cdot\mathbf{n},\mathbf{n},\omega)\,\mathrm{d}\mathbf{n}-\int_{|\mathbf{n}|=1}\bar{J}_k^{(\Gamma)}(\mathbf{x}\cdot\mathbf{n},\mathbf{n},\omega)\,\mathrm{d}\mathbf{n} \tag{59}$$

of the displacement contribution over a unit circle; further reduction to the half-circle integration is possible due to the two-fold symmetry of the integrands. Thus, the burden of numerical integration for the proposed time-harmonic boundary element remains comparable to that for the static counterpart involving quadrature integration over the boundary element. This is a

remarkable advantage for the time-harmonic BEM, which otherwise has to deal with double numerical integrals as shown in Eq. (50).

4.4. Anti-plane strain: case study

4.4.1. Coefficients of boundary integral equations

The displacement contribution (59) from an element in anti-plane strain has the form

$$u_3^N(\mathbf{x},\omega)=\sum_{a=1}^{3} g_a^N(\mathbf{x},\omega)t_{3a}-\sum_{a=1}^{3} h_a^N(\mathbf{x},\omega;\mathbf{v})u_{3a}, \tag{60}$$

where u_{3a} and t_{3a} are the nodal displacement and traction, respectively, and g_a^N and h_a^N are the coefficients of the boundary integral equations given by

$$\begin{aligned} g_a^N(\mathbf{x},\omega)&=g_{ar}^N+\mathrm{i}\,g_{ai}^N=\frac{1}{8\mu\pi^2}\int_{|\mathbf{n}|=1}\mathscr{I}_a^2(\mathbf{x}\cdot\mathbf{n},\mathbf{n},\omega)\,\mathrm{d}\mathbf{n},\\ h_a^N(\mathbf{x},\omega;\mathbf{v})&=h_{ar}^N+\mathrm{i}h_{ai}^N=\frac{1}{8\pi^2}\int_{|\mathbf{n}|=1}\mathbf{n}\cdot\mathbf{v}\mathscr{J}_a^2(\mathbf{x}\cdot\mathbf{n},\mathbf{n},\omega)\,\mathrm{d}\mathbf{n}. \end{aligned} \tag{61}$$

The integrands $\mathscr{I}_a^2(\mathbf{x}\cdot\mathbf{n},\mathbf{n},\omega)$ and $\mathscr{J}_a^2(\mathbf{x}\cdot\mathbf{n},\mathbf{n},\omega)$, defined by Eqs. (55) and (56), consist of the fundamental displacement solution and its higher order (up to third) integrals; they inherit the characteristics, such as the cusp, of the fundamental displacement solutions. The corresponding coefficients of the boundary integral equations, g_a^A and h_a^A, based on the analytic fundamental solutions (40) are obtained by a 60-point Gauss quadrature integration over the element.

4.4.2. Integration scheme

Exploiting the double symmetry of the integrands in Eq. (61) we perform the integration along a half-circle and double the contribution. These integrands have two types of numerical singularity: (1) divide 0 by 0 when $\mathbf{n}=\mathbf{p}_e$ is perpendicular to the element and (2) cusps when the angles $\mathbf{n}=\mathbf{p}_1$ and $\mathbf{p}_2$ become perpendicular to $\mathbf{y}_{(1)}-\mathbf{x}$ and $\mathbf{y}_{(2)}-\mathbf{x}$, respectively, where $\mathbf{y}_{(1)}$ and $\mathbf{y}_{(2)}$ are the end nodes of the element as shown in Fig. 4(a). The cusps occur only in the real parts h_{ar}^N and g_{ar}^N. While both the real and imaginary parts face the divide 0 by 0, the imaginary parts h_{ai}^N and g_{ai}^N can handle this much better than the real parts h_{ar}^N and g_{ar}^N. Fig. 4(b) shows the suggested range of the half-circle integration that starts with the positive direction (i.e., from node 1 to 2) Θ_e of the boundary element $\mathbf{y}_{(1)}\mathbf{y}_{(2)}$. The integration is interrupted at each singularity and, before and after each cusp, the double refinement of the integration step is performed.

4.4.3. Angular and κ_2 dependency of accuracy

Consider a unit boundary element along the x-axis between -0.5 and $+0.5$ and calculate the relative error of the boundary element coefficients (61) along the quarter unit-circle in the first quadrant (Fig. 5). We have identified degradation of accuracy at locations of $\mathbf{x}$ extremely close to the element or its extension. Since the coefficients of the boundary equations are calculated with $\mathbf{x}$ exactly on the element or its extension, but not slightly off, this degradation does not affect the boundary integral equations. The accuracy of the coefficients when $\mathbf{x}$ is on the element or its extension as well as the case when $\mathbf{x}$ is not too close to the element is excellent since the relative error is of the order between 10^{-5} and 10^{-6}.

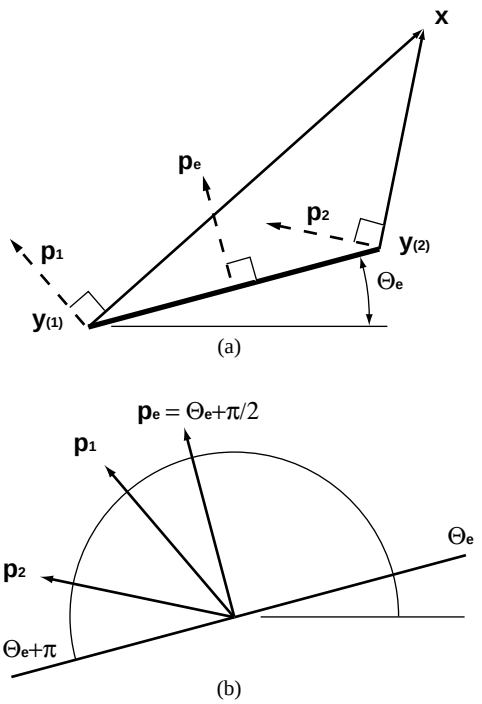

Fig. 4. (a) Geometry of the boundary element $\mathbf{y}_{(1)}\mathbf{y}_{(2)}$ and the source point $\mathbf{x}$ in the determination of critical directions $\mathbf{p}_1$, $\mathbf{p}_2$ and $\mathbf{p}_e$; (b) integration scheme along the half-unit circle.

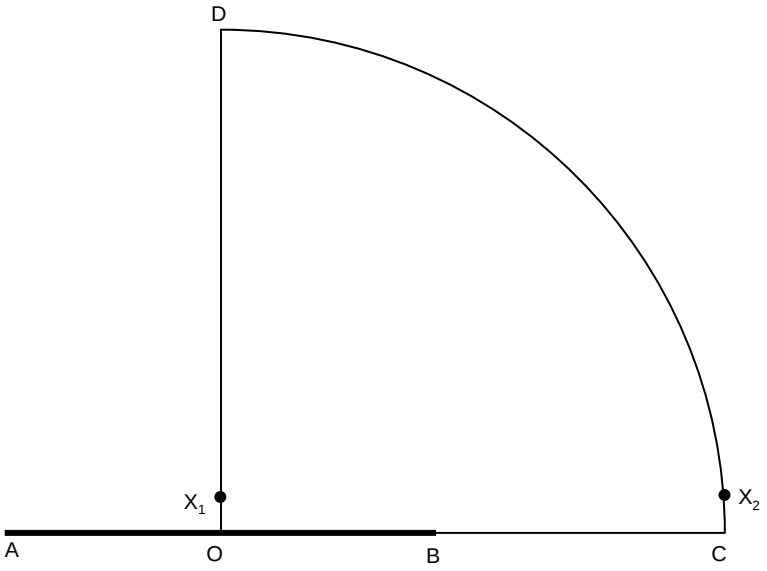

Fig. 5. Unit boundary element on the x-axis and a quarter circular path.

Table 2
Relative error of the boundary element coefficients

	Relative error			
	g_{ar}^N	h_{ar}^N	g_{ai}^N	h_{ai}^N
$0 \leqslant \kappa_2 \leqslant 2$	10^{-8}	10^{-7}	10^{-9}	10^{-7}
$0 \leqslant \kappa_2 \leqslant 10$	10^{-7}	10^{-6}	10^{-9}	10^{-7}
$0 \leqslant \kappa_2 \leqslant 20$	10^{-6}	10^{-5}	10^{-8}	10^{-7}
$20 \leqslant \kappa_2 \leqslant 40$	10^{-5}	10^{-4}	10^{-7}	10^{-6}
$40 \leqslant \kappa_2 \leqslant 60$	10^{-4}	10^{-3}	10^{-7}	10^{-6}

Next, we have calculated the relative error along the perpendicular bi-sector of the same element. Let r be the distance from the point on the bi-sector to one of the end nodes of the element. As $\mathbf{x}$ moves along the bi-sector the parameter $\kappa_2 = k_2 r$ increases. To accommodate an increasing value of κ_2 we have used the guideline for n (number of sub-intervals along the half-circle) set by Eq. (46) and used the value of q (number of quadrature points for the real part) set in Table 1. The value of p (number of quadrature points for the imaginary part) did not follow Table 1, instead we have used the same value as q. Table 2 shows the relative error of the boundary element coefficients in various ranges of κ_2.

5. Eigenvalue analysis

5.1. Non-linear eigenvalue problem and QZ algorithm

The system of boundary equations resulting from the direct displacement formulation has the form

$$[\mathbf{H}(\omega)]\{\mathbf{u}\} - [\mathbf{G}(\omega)]\{\mathbf{t}\} = \{\mathbf{0}\}, \tag{62}$$

where $[\mathbf{H}(\omega)]$ and $[\mathbf{G}(\omega)]$ are $N \times N$ matrices and $\{\mathbf{u}\}$ and $\{\mathbf{t}\}$ are the boundary displacement and traction vectors. The form of the eigenvalue problem for the homogeneous boundary condition is

$$[\mathbf{Q}(\omega)]\{\mathbf{r}\} = \{\mathbf{0}\}, \tag{63}$$

where $[\mathbf{Q}(\omega)]$ is a $N \times N$ matrix and $\{\mathbf{r}\}$ is $N \times 1$ boundary value vector consisting of non-zero displacement and traction components. For example, for the displacement (i.e., $\{\mathbf{u}\} = \{\mathbf{0}\}$) and the traction (i.e., $\{\mathbf{t}\} = \{\mathbf{0}\}$) boundary value problems we have

$$[\mathbf{G}(\omega)]\{\mathbf{t}\} = \{\mathbf{0}\} \tag{64}$$

and

$$[\mathbf{H}(\omega)]\{\mathbf{u}\} = \{\mathbf{0}\}, \tag{65}$$

respectively.

The components of the matrix $[\mathbf{Q}(\omega)]$ in Eq. (63) are non-linear complex-values functions of the eigenfrequency ω. Kitahara [2] determined the eigenfrequencies by calculating $\det[\mathbf{Q}(\omega)]$ at

multiple values of ω in a given interval; this is called the direct search method. The local minima, instead of zeros, of the determinant are achieved at the eigenfrequencies. The accuracy of this method is strongly influenced by the increment size $\Delta\omega$ and it is inefficient. We propose a procedure using the QZ algorithm below [12–14]. First, set up an interval $[\omega_A, \omega_B]$, where we approximate $[\mathbf{Q}]$ by a matrix polynomial of order M to get an approximate eigenvalue problem

$$[[\mathbf{Q}_0] + \omega[\mathbf{Q}_1] + \omega^2[\mathbf{Q}_2] + \cdots + \omega^M[\mathbf{Q}_M]]\{\mathbf{r}\} = \{\mathbf{0}\}. \tag{66}$$

The $N \times N$ coefficient matrices $[\mathbf{Q}_0]$, $[\mathbf{Q}_1], \ldots, [\mathbf{Q}_M]$ are obtained by Newton's divided differences in the interval $[\omega_A, \omega_B]$. If we introduce a new series of vectors

$$\{\mathbf{r}_i\} = \omega^i\{\mathbf{r}\} \quad (i = 0, 1, \ldots, M), \tag{67}$$

then Eq. (66) can be written as

$$[\mathbf{Q}_0]\{\mathbf{r}_0\} + [\mathbf{Q}_1]\{\mathbf{r}_1\} + [\mathbf{Q}_2]\{\mathbf{r}_2\} + \cdots + [\mathbf{Q}_M]\{\mathbf{r}_M\} = \{\mathbf{0}\}. \tag{68}$$

Eq. (68) is equivalent to a linear general eigenvalue problem,

$$[\tilde{\mathbf{Q}}]\{\tilde{\mathbf{r}}\} = \omega[\tilde{\mathbf{P}}]\{\tilde{\mathbf{r}}\}, \tag{69}$$

where $[\tilde{\mathbf{Q}}]$ and $[\tilde{\mathbf{P}}]$ are $MN \times MN$ matrices and $\{\tilde{\mathbf{r}}\}$ is a $MN \times 1$ vector defined by

$$[\tilde{\mathbf{Q}}] = \begin{bmatrix} [\mathbf{Q}_{M-1}] & [\mathbf{Q}_{M-2}] & \cdots & [\mathbf{Q}_2] & [\mathbf{Q}_1] & [\mathbf{Q}_0] \\ [\mathbf{I}] & [\mathbf{0}] & \cdots & [\mathbf{0}] & [\mathbf{0}] & [\mathbf{0}] \\ [\mathbf{0}] & [\mathbf{I}] & \cdots & [\mathbf{0}] & [\mathbf{0}] & [\mathbf{0}] \\ \cdots & \cdots & \cdots & \cdots & \cdots & \cdots \\ [\mathbf{0}] & [\mathbf{0}] & \cdots & [\mathbf{I}] & [\mathbf{0}] & [\mathbf{0}] \\ [\mathbf{0}] & [\mathbf{0}] & \cdots & [\mathbf{0}] & [\mathbf{I}] & [\mathbf{0}] \end{bmatrix},$$

$$[\tilde{\mathbf{P}}] = \begin{bmatrix} -[\mathbf{Q}_M] & [\mathbf{0}] & [\mathbf{0}] & \cdots & [\mathbf{0}] & [\mathbf{0}] \\ [\mathbf{0}] & [\mathbf{I}] & [\mathbf{0}] & \cdots & [\mathbf{0}] & [\mathbf{0}] \\ [\mathbf{0}] & [\mathbf{0}] & [\mathbf{I}] & \cdots & [\mathbf{0}] & [\mathbf{0}] \\ \cdots & \cdots & \cdots & \cdots & \cdots & \cdots \\ [\mathbf{0}] & [\mathbf{0}] & [\mathbf{0}] & \cdots & [\mathbf{I}] & [\mathbf{0}] \\ [\mathbf{0}] & [\mathbf{0}] & [\mathbf{0}] & \cdots & [\mathbf{0}] & [\mathbf{I}] \end{bmatrix}, \quad [\tilde{\mathbf{r}}] = \begin{Bmatrix} \omega^{M-1}\{\mathbf{r}\} \\ \omega^{M-2}\{\mathbf{r}\} \\ \omega^{M-3}\{\mathbf{r}\} \\ \cdots \\ \omega\{\mathbf{r}\} \\ \{\mathbf{r}\} \end{Bmatrix}, \tag{70}$$

where $[\mathbf{I}]$ and $[\mathbf{0}]$ are $N \times N$ identity and zero matrices. Eq. (69) can be solved by the QZ algorithm [12]. Notice that the QZ algorithm always provides MN eigenvalues for each interval $[\omega_A, \omega_B]$ of search. These eigenvalues all satisfy Eq. (69), but most of them are spurious, which are identified by complex-valued or real-valued eigenvalues outside the interval $[\omega_A, \omega_B]$. The physical requirement for real-valued eigenvalues forces us to throw away all spurious eigenvalues. Since the real eigenvalues seldom occur in the analysis and they usually come with small imaginary numbers, we pick up the true eigenvalues using the criterion: (1) the imaginary part is less than a

small number ε to be discussed below and (2) the real part is in the interval $[\omega_A, \omega_B]$. If the real part of an eigenvalue with a small imaginary part, selected by (1), lies outside the interval, then it actually belong to an adjacent interval, where its value is calculated more accurately. Thus we discard such eigenvalue as spurious according to (2) above.

5.2. Anti-plane strain: case study

5.2.1. Direct search method for square region

Consider a square isotropic domain of size a. The eigenmodes for the displacement zero BC are given by the products of $\cos[(2p-1)\pi/a]x$ or $\sin(2p\pi/a)x$ in the x direction and $\cos[(2q-1)\pi/a]y$ or $\sin(2q\pi/a)y$ in the y direction, where p and q are positive integers. The non-dimensional eigenvalues are given by

$$\bar{k}_2 = ak_2 = \pi\sqrt{m^2+n^2}, \tag{71}$$

where $m = 2p-1, 2p$ and $n = 2q-1, 2q$ are positive integers. Similarly the eigenmodes for the traction zero BC are given by the products of $\sin[(2p+1)\pi/a]x$ or $\cos(2p\pi/a)x$ in the x direction and $\sin[(2q+1)\pi/a]y$ or $\cos(2q\pi/a)y$ in the y direction, where p and q are non-negative integers. The non-dimensional eigenvalues are still given by Eq. (71) with m and n being non-negative integers (i.e., 0 is allowed). The integers m and n indicate the number of half-wavelength in x and y directions, respectively. Note that we use the wave number k_2 instead of the angular frequency ω; they are related linearly by $k_2 = \omega/c_2$, where c_2 is the shear wave speed.

First, consider the case for $m = 1$. Figs. 6(a) and (b) show approximation of half-wavelengths $\cos(\pi/a)x$ (displacement zero BC) and $\sin(\pi/a)x$ (traction zero BC) by the quadratic boundary element along the boundary. We see that, although the quadratic interpolation can approximate the half-wavelengths in both cases, the former is more accurate than the latter. In general, for mth order eigenmode in x and y directions, we need to use m boundary elements in both directions. However, the eigen modes for displacement zero BC can be represented more accurately than those for traction zero BC. We have introduced six different meshes, MESH-m ($m = 1, \ldots, 6$) with m elements on each side of the square, and determined its eigenfrequencies by the direct search method to be compared with the analytic results given by Eq. (71). We expect that the finest mesh, MESH-6, can represent up to sixth order eigenmodes in x and y directions accurately; the

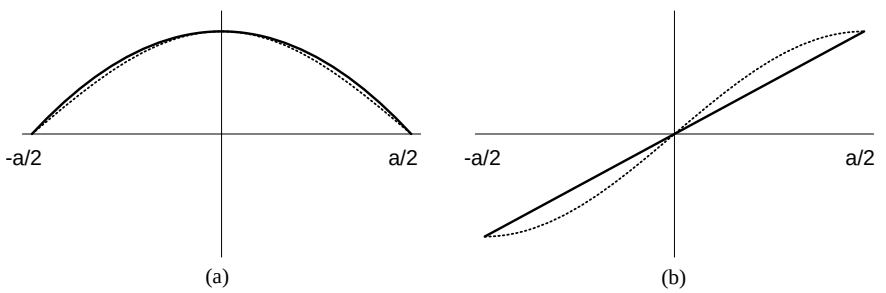

Fig. 6. Approximation (solid line) of eigenmodes (a) $\cos(\pi/a)x$ (displacement zero) and (b) $\sin(\pi/a)x$ (traction zero) by the quadratic interpolation.

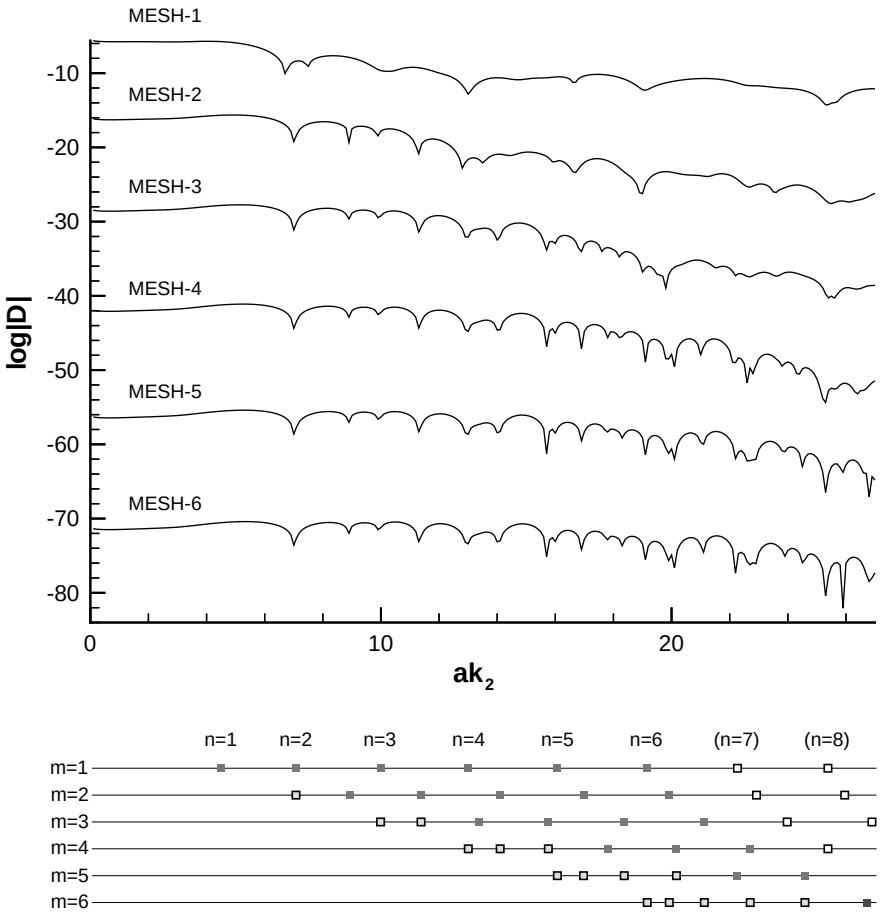

Fig. 7. Determinant of $[\mathbf{G}(\bar{k}_2)]$ as the function of $\bar{k}_2$ for MESH-m ($m = 1, \ldots, 6$) for displacement zero BC. Theoretical eigenvalues are listed below: solid and shaded squares are eigenvalues for $m, n \leqslant 6$.

maximum eigenvalue predictable accurately is expected to be $\bar{k}_2^{max} = \pi\sqrt{6^2 + 6^2} \approx 26.657298$. Figs. 7 and 8 show variation of the absolute values of the determinants $[\mathbf{G}(\bar{k}_2)]$ (for displacement zero) and $[\mathbf{H}(\bar{k}_2)]$ (for traction zero) as the functions of the non-dimensional wave number $\bar{k}_2$ in the range $0 \leqslant \bar{k}_2 \leqslant 27$ using the increment $\Delta\bar{k}_2 = 0.1$.

For each determinant curve the locations of the eigenvalues are indicated by the local minima of the absolute value of the determinant but not zeroes. The direct search method is time consuming since determinant values for non-eigenvalues must also be calculated and the result is critically dependent on the increment size $\Delta\bar{k}_2$. The accuracy of the eigen values is only as good as the increment size. For the eigenvalue analysis of the completely unknown problem, the optimum increment size $\Delta\bar{k}_2$ must be determined after several trials and there is no guarantee that all eigenvalues have been picked out in the range of $\bar{k}_2$ considered. Nevertheless, the direct search method is a useful technique to initially identify approximate locations of the eigenvalues up to the accuracy of the increment.

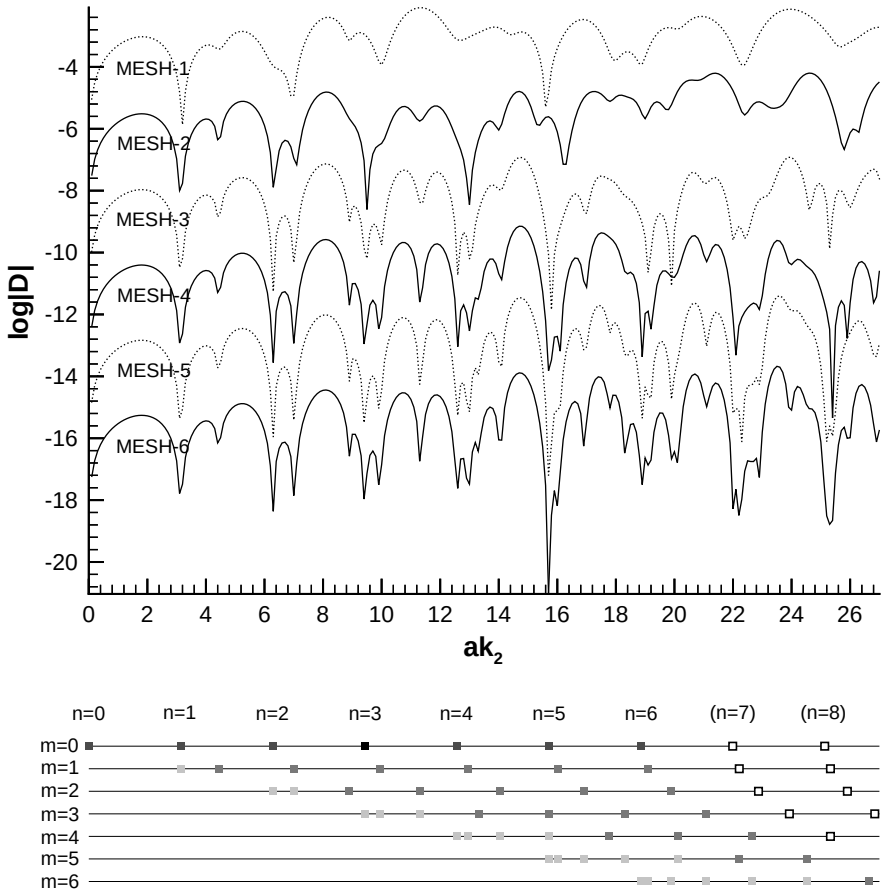

Fig. 8. Determinant of $[\mathbf{H}(\bar{k}_2)]$ as the function of $\bar{k}_2$ for MESH-m ($m = 1, \ldots, 6$) for traction zero BC. Theoretical eigenvalues are listed below: solid and shaded squares are eigenvalues for $m, n \leqslant 6$.

5.2.2. QZ algorithm for square region

We assume, for now, that all the eigenvalues in the region considered have been picked up by the direct search method with the increment $\Delta\bar{k}_2$, used in the direct search, and the locations of the local minima are identified. Let $\bar{k}_2^{(i)}$ be the ith minimum for either displacement or traction zero BC. We propose to apply the QZ algorithm introduced in Section 5.1 for the interval $(\bar{k}_2^{(i)} - \Delta\bar{k}_2, \bar{k}_2^{(i)} + \Delta\bar{k}_2)$, where the presence of at least one eigenvalue is guaranteed, using the matrix polynomial of order $M = 2$ in Eq. (66) to improve the accuracy of the eigenvalue $\bar{k}_2^{(i)}$. In each interval the QZ algorithm produces total of $2N$ eigenvalues of Eq. (69) most of which are spurious eigenvalues. While the eigenvalues we are looking for have real values, the spurious eigenvalues are either complex-valued or, if real, lie outside the interval $(\bar{k}_2^{(i)} - \Delta\bar{k}_2, \bar{k}_2^{(i)} + \Delta\bar{k}_2)$. Thus we look for eigenvalues with the real parts within this interval and small imaginary parts. Specifically, we look for the eigenvalue $(\bar{k}_2^{(i)} + \delta^{(i)}) + i\varepsilon^{(i)}$, where $\delta^{(i)}$ (improvement in the real part) and $\varepsilon^{(i)}$ (imaginary part) are small real numbers. Although this eigenvalue still has a small imaginary part, we accept its real part $(\bar{k}_2^{(i)} + \delta^{(i)})$ as the improved version of the eigenvalue $\bar{k}_2^{(i)}$. More important,

the value of $\varepsilon^{(i)}$ that goes with the true eigenvalue gives an indication on the size of threshold ε used to cut-off other complex-valued eigenvalues as spurious. Our numerical results have indicated that only a few eigenvalues have small imaginary numbers and all others have large imaginary parts of order 10 or more times the size of $\varepsilon^{(i)}$. So the distinction of the true from spurious eigenvalues has been straightforward. In addition, if the real parts of the selected eigenvalues are outside of the interval $(\bar{k}_2^{(i)} - \Delta\bar{k}_2, \bar{k}_2^{(i)} + \Delta\bar{k}_2)$, then we discard them as spurious since they belong to the adjacent search intervals, where more accurate values can be obtained than in the current interval. Comparison of the results with theory (71) indicates that the displacement and traction zero boundary conditions give at least 4 and 3 significant digits agreement in the eigen values with the theoretical values.

6. Numerical results

6.1. Controlling parameter in eigenvalue analysis

The outcome of the error analysis in Sections 3.3, 4.4 and 5.2 for the anti-plane strain isotropic problem will be used here to solve the generalized plane strain problems. In generalized plane strain the fundamental solutions depend on

$$\kappa_m = k_m r, \tag{72}$$

where $r = |\mathbf{y} - \mathbf{x}|$ and k_m $(m = 1, 2, 3)$ is the wave number defined by Eq. (16). Let $\bar{k}_m$, $\bar{\omega}$, $\bar{c}_m$ and $\bar{r}$ be non-dimensional wave number, angular frequency, phase velocity and distance, respectively, defined by

$$\bar{k}_m = ak_m, \quad \bar{\omega} = a\omega/c_2, \quad \bar{c}_m = c_m/c_2, \quad \bar{r} = r/a, \tag{73}$$

where $c_2 = \sqrt{c_{66}/\rho}$ is the shear wave speed and a is the characteristic length of the problem. We can rewrite Eq. (72) as

$$\kappa_m = k_m r = \bar{k}_m \bar{r}, \tag{74}$$

where

$$\bar{k}_m = \bar{\omega}/\bar{c}_m \tag{75}$$

is the non-dimensional wave number which, along with $\bar{c}_m$, varies over the unit circle $|\mathbf{n}| = \mathbf{1}$. Fig. 9 shows plots of $1/\bar{c}_m$ for (a) iron (isotropic), (b) zinc oxide (hexagonal), (c) aluminum crystal (cubic) and (d) AT-cut quartz. Since the variation of $1/\bar{c}_m$ is generally contained in the neighborhood of 1, we can replace Eq. (75) by

$$\bar{k}_m \sim \bar{\omega} \tag{76}$$

so that Eq. (74) is given by

$$\kappa_m \sim \bar{\omega}\bar{r} \tag{77}$$

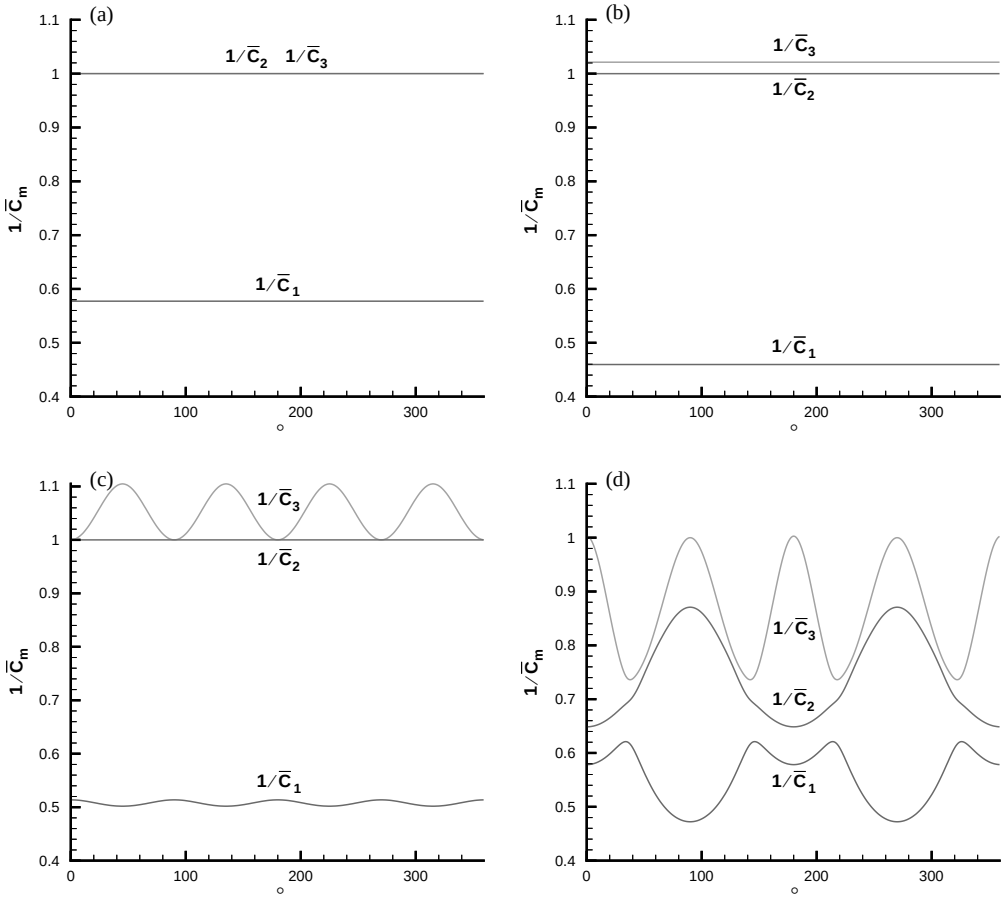

Fig. 9. Plots, along the unit-circle, of $1/\bar{c}_m$ for (a) iron (isotropic), (b) zinc oxide (hexagonal), (c) aluminum crystal (cubic) and (d) AT-cut quartz. The non-dimensional velocities $\bar{c}_1$, $\bar{c}_2$ and $\bar{c}_3$ are longitudinal and two shear wave velocities, respectively.

for $m = 1, 2, 3$. Thus $\bar{\omega}$ can be used as the controlling parameter in the eigenvalue analysis. Once eigenvalues for $\bar{\omega}$ are obtained we can get the actual radial frequency by

$$\omega = \frac{c_2}{a}\bar{\omega}. \tag{78}$$

6.2. Square domain: generalized plane strain

We have analyzed a square domain of size a for AT-cut quartz using MESH-6 of Section 5.2.1 with 24 elements and 48 nodes. The search range considered is $0.0 \leqslant \bar{\omega} \leqslant 20.0$ with $n = 9$ and the number of Gauss quadrature points is 8. First, we have applied the direct search method a few times with different $\bar{\omega}$ increment sizes to get the approximate locations of the eigenvalues in this range. This information is used to determine the sub-interval size $\Delta\bar{\omega}$ in the QZ-algorithm. A large sub-interval, which may contain multiple eigenvalues, requires a high value such as $M = 5$ in

Eq. (66), which is computationally costly. A better strategy is to use a low value such as $M = 1$ for a small sub-interval. The latter strategy requires a larger number of sub-intervals, but computation for each sub-interval is much faster than the former since the size of the matrices in Eq. (66) is 720 and 144 for $M = 5$ and 1, respectively. Thus we have abandoned the two-step

Table 3
Eigenfrequencies for a square AT-Cut quartz domain with displacement zero BC

BEM		FEM	
$\Delta\bar{\omega} = 0.125$	$\Delta\bar{\omega} = 0.05$	25 Elements	4 Elements
6.0078621	6.0077591	6.0076879	6.0076882
6.2608666	6.2607163	6.2606436	6.2606486
7.3603363	7.3601248	7.3599831	7.3599866
8.1828851	8.1823605	8.1823982	8.1824449
8.6754927	8.6750733	8.6749964	8.6750407
9.1434493	9.1431803	9.1432205	9.1432859
10.390321	10.390187	10.390173	10.390239
10.813610	10.813183	10.813485	10.814858
11.256492	11.256445	11.256479	11.256564
11.326389	11.325965	11.326460	11.327588
11.844321	11.844043	11.844122	11.845733
12.018874	12.018719	12.018889	12.019000
12.616882	12.616832	12.617211	12.617773
13.532676	13.532455	13.532471	13.532701
13.638612	13.638519	13.639268	13.643142
14.083201	14.082865	14.084242	14.088313
14.295053	14.294717	14.295843	14.296945
14.488844	14.488750	14.489533	14.490908
14.654810	14.654579	14.655000	14.655818
14.993935	14.993899	14.993949	14.996243
15.214765	15.214546	15.214803	15.218835
15.820995	15.820684	15.821716	15.824148
16.419473	16.419154	16.422267	16.428103
16.521996	16.521880	16.522349	16.534820
16.594179	16.593967	16.595284	16.731951
16.728244	16.728104	16.729384	16.745604
16.942111	16.941781	16.944663	17.101065
17.346473	17.346232	17.348238	17.353431
17.368696	17.368681	17.369626	17.373787
17.760638	17.760569	17.764048	17.769456
18.027522	18.027354	18.028989	18.032073
18.670055	18.669873	18.670554	18.859235
18.954457	18.954115	18.960464	19.102826
19.098938	19.098731	19.102645	19.108244
19.569656	19.569433	19.568221	missed
19.722122	19.722002	19.722133	19.727702
19.848450	19.848240	19.847561	missed
19.993377	19.993331	19.996622	19.969102

Table 4
Eigenfrequencies for a square AT-Cut quartz domain with traction zero BC

BEM		FEM	
$\Delta\bar{\omega} = 0.125$	$\Delta\bar{\omega} = 0.05$	25 Elements	4 Elements
3.5991203	3.5993905	3.5993212	3.5993213
3.9200069	3.9202453	3.9199152	3.9199467
4.3388588	4.3395542	4.3386493	4.3387021
4.8472878	4.8473558	4.8473166	4.8473177
4.8657352	4.8658312	4.8642374	4.8643740
5.3914851	5.3915252	5.3914491	5.3914492
6.0088374	6.0089080	6.0088437	6.0088446
6.0143505	6.0146279	6.0132876	6.0133099
6.6858113	6.6857881	6.6856712	6.6856713
6.8408549	6.8409950	6.8396530	6.8398026
7.2441487	7.2441563	7.2436488	7.2436617
7.5559054	7.5560045	7.5549415	7.5550866
missed	7.6789820	7.6701030	7.6710782
8.6559273	8.6561644	8.6553847	8.6554587
9.0462354	9.0467825	9.0356755	9.0399610
9.2259863	9.2262870	9.2121759	9.2146103
9.3594178	9.3595094	9.3530747	9.3542897
9.3716618	9.3715970	9.3601576	9.3622508
9.7056323	9.7057153	9.7043710	9.7045917
10.363739	10.363728	10.362191	10.362466
10.821954	10.822052	10.819737	10.821639
10.871366	10.871359	10.871112	10.871123
11.395315	11.395295	11.392039	11.393152
11.483380	11.483517	11.444225	11.459929
11.675887	11.676468	11.642673	11.683010
11.693935	11.694416	11.674124	11.696642
11.916374	11.916680	11.903352	11.921719
12.012801	12.012889	12.012237	12.012458
12.710070	12.710114	12.690238	12.695667
12.824293	12.824343	12.803503	12.811609
13.301219	13.301247	13.300681	13.300697
13.439162	13.439765	13.387852	13.463345
13.583888	13.584021	13.560337	13.577632
14.162303	14.162529	14.118103	14.156795
14.460761	14.460708	14.410169	14.471344
14.468639	14.468687	14.454755	14.483490
14.471720	14.471573	14.469865	14.503652
14.537237	14.537405	14.530465	14.541444
14.748690	14.748408	14.686968	14.747795
14.981675	14.981639	14.971744	14.980332
15.072531	15.072770	15.008505	15.147384
15.139508	15.140088	15.077389	15.154354
15.263604	15.263996	15.248540	15.325252
15.955163	15.955192	15.943572	16.007304
16.290997	16.291039	16.221189	16.292242
16.295308	16.295900	16.289445	16.379562

Table 4 (*continued*)

BEM		FEM	
$\Delta\bar{\omega} = 0.125$	$\Delta\bar{\omega} = 0.05$	25 Elements	4 Elements
16.417150	16.417222	16.388288	16.434174
16.646910	16.646904	16.636428	16.701171
16.963276	16.963301	16.926094	17.038081
17.132414	17.132957	16.966781	17.147070
17.370950	17.370266	17.361264	17.419562
17.516781	17.517728	17.707722	17.536129
17.905002	17.905738	17.740458	18.014818
17.966565	17.965849	17.930135	18.022019
17.979249	17.978643	18.016519	18.114717
18.022839	18.023245	18.034284	18.164537
18.046577	18.047013	18.582509	18.224731
18.689240	18.689638	18.672291	18.830472
missed	18.750517	19.2125	18.862395
19.244393	19.244450	19.333551	19.344924
19.377319	19.377436	19.373203	19.447317
19.433399	19.433580	19.508725	19.666257
19.579222	19.579190	19.867892	19.680866
19.938584	19.938964	19.970848	19.972644
19.975327	19.975341	19.991958	20.099036

search (i.e., the initial global and final local) in favor of the one-step search by the QZ algorithm using $M = 1$ and the small sub-interval size.

After selecting the sub-interval size, we have run the QZ-algorithm in the first few sub-intervals i $(= 1, 2, \ldots)$ in each of which the presence of at least one eigenvalue, say $\bar{\omega}^{(i)}$, is guaranteed by the direct search. Indeed, the QZ algorithm always finds the corresponding eigenvalue with the improved real part $\bar{\omega}^{(i)} + \delta^{(i)}$ and a small imaginary part $\varepsilon^{(i)}$ in each interval. It may also find a few new eigenvalues with small imaginary parts but their real parts have usually been outside the current search range. The other majority of the eigenvalues have imaginary parts one order or more larger than $\varepsilon^{(i)}$. The last two groups of eigenvalues are spurious and must be discarded. Most important, we use the values of the small imaginary parts $\varepsilon^{(i)}$ $(i = 1, 2, \ldots)$ associated with the true eigenvalues to determine the threshold value ε used in the subsequent selection of the true eigenvalues. Thus the criterion used to pick up the true eigenvalues is: (1) the absolute value of the imaginary part is less than $\varepsilon = 0.1$ and (2) the real part is in the search region. We have performed two sets of searches using two sub-interval sizes, $\Delta\bar{\omega} = 0.125$ and 0.05. Two different searches with different sub-interval sizes were used to avoid missing eigenvalues located in the extreme neighborhood of some of the sub-intervals. Tables 3 and 4 list eigenvalues found for displacement and traction zero BCs for two sub-interval sizes. Notice that two eigenvalues missed by the sub-interval $\Delta\bar{\omega} = 0.125$ were picked up by the use of a sub-interval of 0.05. These tables also list two-sets of results by the FEM which has used four and twenty-five 36-nodes elements, respectively; the total number of nodes for the FEM calculation are 121 and 676, respectively. The FEM 36-nodes element has 20 and 16 nodes on and inside the boundary, respectively; it covers the element uniformly by a 6×6 array of nodes. The current FEM, developed by Wang et al. [1], has been

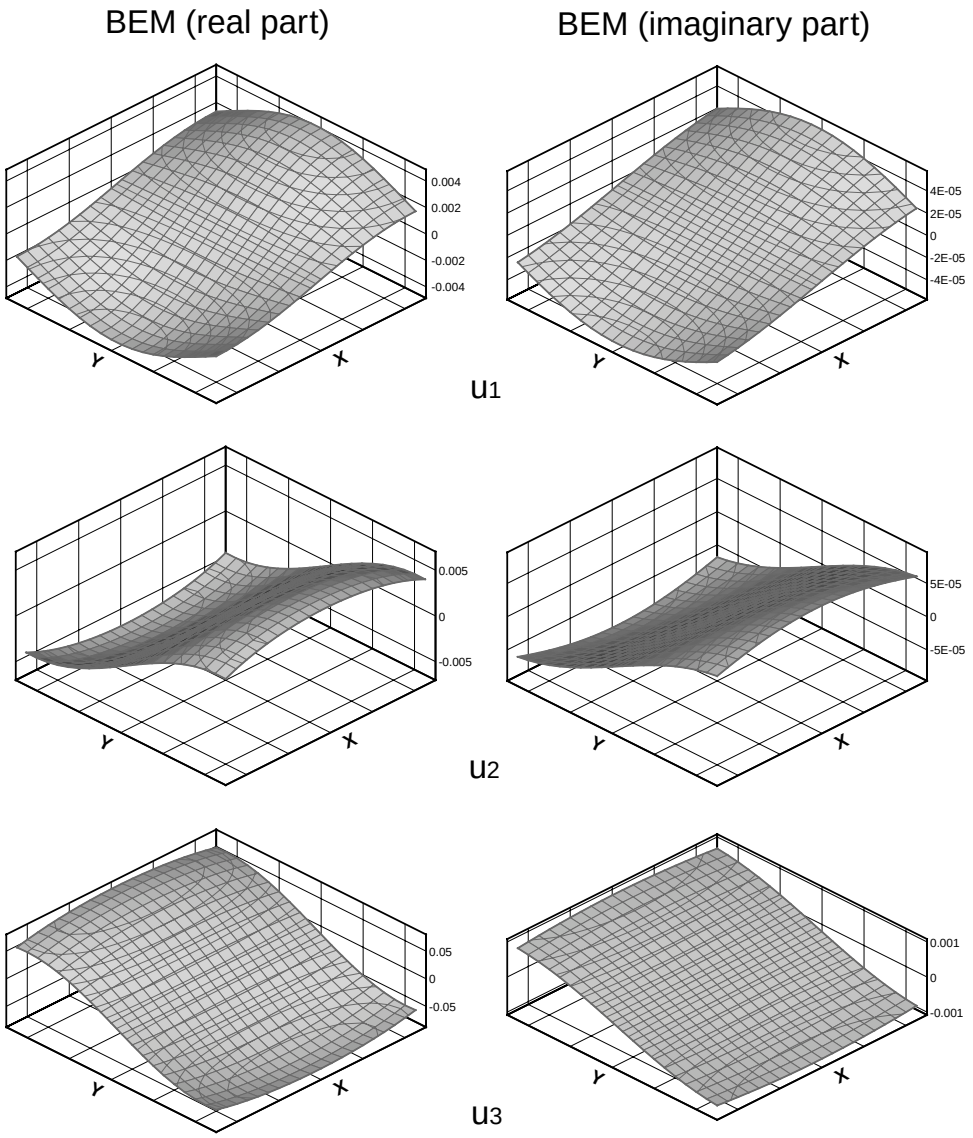

Fig. 10. 3-D plots of real and imaginary parts of displacement components obtained by the BEM: $\bar{\omega} = 3.5993905$ for traction zero BC.

used for industrial applications in the frequency range $\bar{\omega} < 2$ and is considered to be the best in the low-frequency eigenvalue analysis for general anisotropic/piezoelectric solids. The BEM and FEM results agree up to 5 and 4 digits for $\bar{\omega} < 10$ of displacement and traction zero BCs, respectively. The performance of the FEM deteriorates for $\bar{\omega} > 15$. This is the range where the FEM results have improved significantly from four to 25 elements; the improved results have approached those by the BEM indicating that the BEM results are more accurate in this range. The FEM using four elements has missed two eigenvalues, which have eventually been identified

by using 25 elements; the BEM has never missed these two. Further, the FEM results for traction zero BCs show some irregularity in this range. For the majority of industrial applications, the range of frequency is $\bar{\omega}<2$; the agreement of the BEM and FEM is excellent in this range. However, as more higher frequency applications appear, such as the SAW using diamond, the importance of the higher frequency capability of the BEM should stand out.

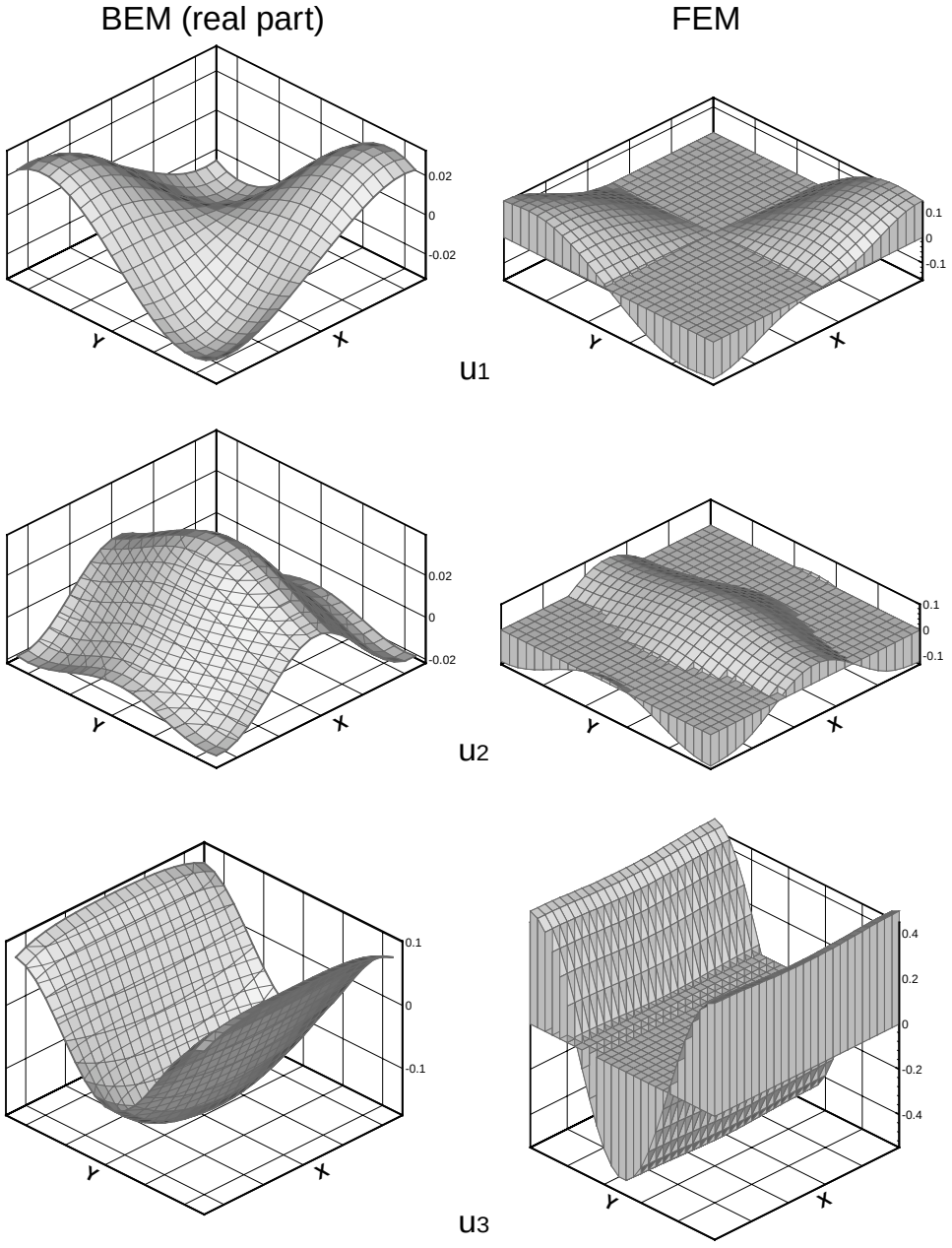

Fig. 11. 3-D plots for the eigenfrequency 6.0089080 (traction zero BC) obtained by the BEM (real part) and the FEM.

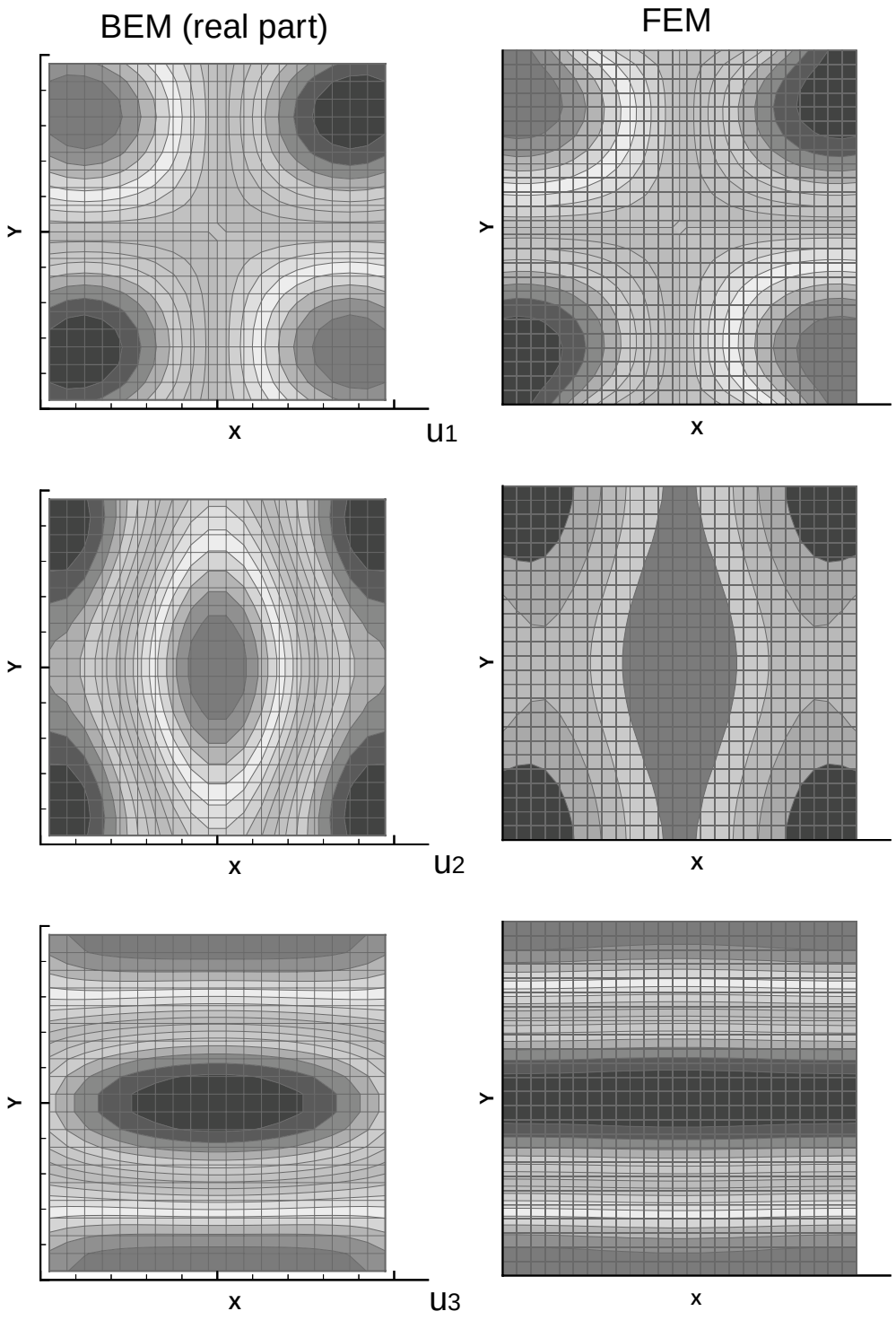

Fig. 12. 2-D plots for the eigenfrequency 6.0089080 (traction zero BC) obtained by the BEM (real part) and the FEM.

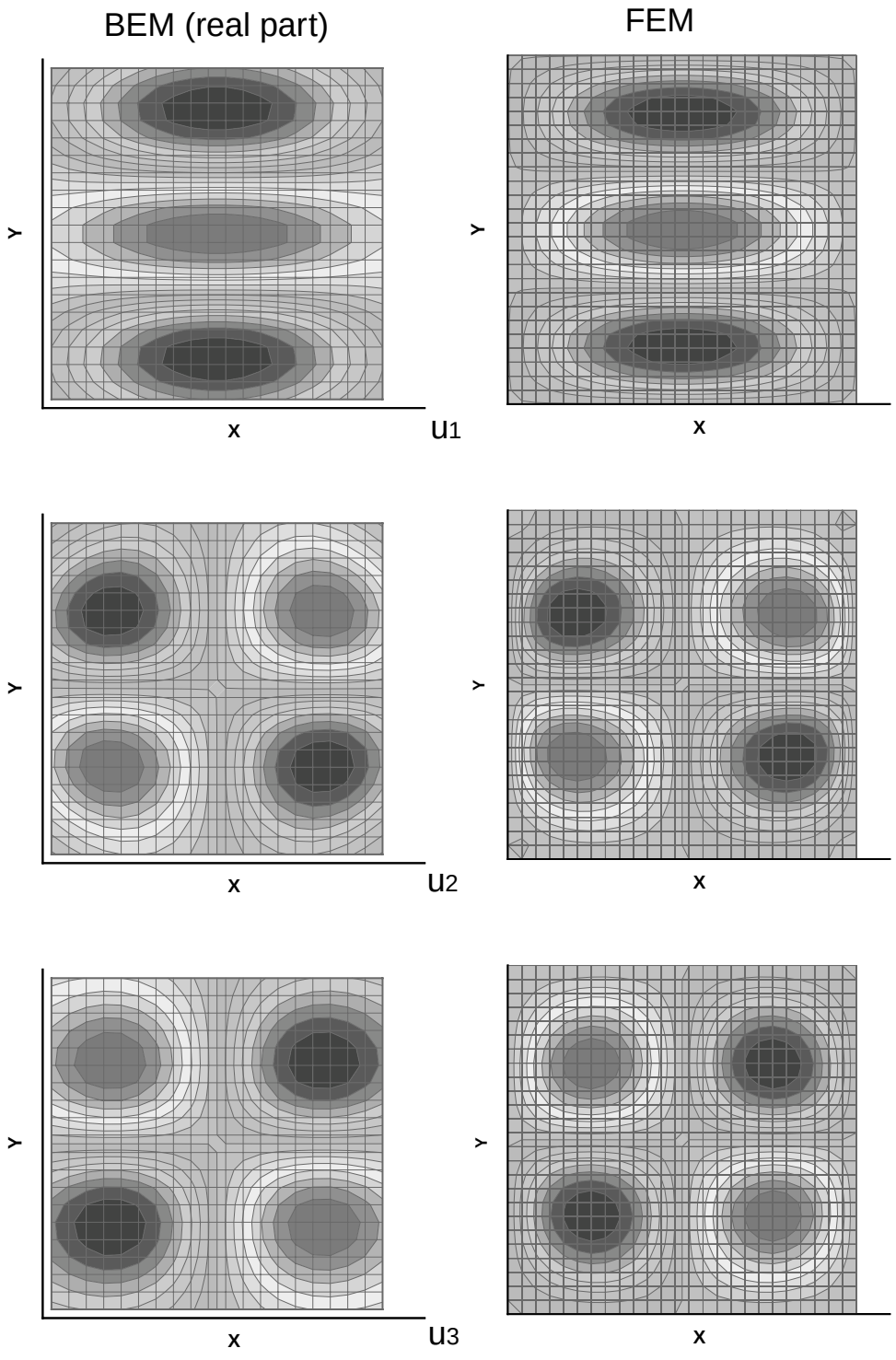

Fig. 13. 2-D contour plots for displacement zero eigenfrequency 10.813183 obtained by the BEM and the FEM.

Figs. 10–13 show eigen modes of displacements for four selected eigenvalues for displacement and traction zero BCs calculated by the BEM and the FEM. The displacement fields by the BEM have been calculated using the eigenvector which is normalized to have an Euclidean length equal to one, while the FEM results are normalized by the maximum displacement component in the field.

Fig. 10 shows 3D plots of the real and imaginary parts of the displacement components (u_1, u_2 and u_3) by the BEM; the eigenfrequency is $\bar{\omega} = 3.5993905$ for traction zero BC. Figs. 11 and 12 show 3D and 2D contour plots for the eigenfrequency 6.0089080 (traction zero BC) obtained by the BEM (real part) and the FEM. Although a slight distortion of the BEM results near the boundary region is observed, the basic agreement between the two results is satisfactory. Fig. 13 shows 2-D contour plots for a displacement zero eigenfrequency of 10.813183 obtained by the BEM and the FEM. Notice the basic agreement between the two results; the disagreement in the near boundary region is caused by the inability of the BEM to calculate the accurate solution in the immediate neighborhood of the boundary as pointed out in Section 4.4.3. While the FEM results are plotted in the full field, i.e., $-0.5 \leqslant x \leqslant 0.5$ and $-0.5 \leqslant y \leqslant 0.5$, the BEM results are plotted in the region $-0.475 \leqslant x \leqslant 0.475$ and $-0.475 \leqslant y \leqslant 0.475$ to avoid the loss of accuracy in the near boundary region.

7. Concluding remarks

We have developed a time-harmonic BEM for general anisotropic solids in 2-D using the fundamental solution obtained by the Radon transform. The evaluation of the boundary element coefficients is reduced to the line integral over the unit circle. The error analysis has established guidelines for the accurate numerical evaluation of the line integrals. We have applied the BEM to the eigenvalue analysis using the QZ algorithm. When no prior information on the distribution of the eigenvalues is available, the direct search method should be used prior to the QZ algorithm to determine the approximate locations of the eigenvalues and the sub-interval size used for the QZ algorithm. For the QZ algorithm, the linear approximation ($M = 1$) of the non-linear matrix along with the small sub-interval size should be used. It is recommended that two sets of searches with different sub-interval sizes are used to eliminate the possibility of missing eigenvalues located near the sub-interval boundary. Most of the eigenvalues obtained by the QZ algorithm in a given sub-interval are spurious. The true eigenvalues are identified by requiring that the real parts are in the sub-interval and the imaginary parts are less than a small number ε.

The eigenfrequency results are in agreement with the most reliable FEM results to several significant digits. The proposed BEM implementation combined with the non-linear eigenvalue solver provides a reliable platform for the computation of eigenfrequencies for solids with general anisotropy. It is a strong candidate to replace the traditional dual reciprocity BEM (DRBEM) and FEM designed for the eigenvalue problems. The proposed BEM is generally applicable to a wider class of two-dimensional time-harmonic problems not limited to the eigenvalue analysis.

Acknowledgements

The boundary element formulation, implementation and analysis were performed by Denda and Wang. The finite element analysis was performed by Yong and his graduate student Mr. Wei Wu. Denda and Yong acknowledge the support by Seiko-Epson, Inc. Wang acknowledges Schlumberger-Doll Research for time released to stay at Rutgers University as a visiting scholar.

References

[1] J. Wang, Y.-K. Yong, T. Imai, Finite element analysis of the piezoelectric vibrations of quartz plate resonators with higher order plate theory, International Journal of Solids and Structures 36 (1999) 2303–2319.
[2] M. Kitahara, Boundary Integral Equation Methods in Eigenvalue Problems of Elastodynamics and Thin Plates, Elsevier, Amsterdam, 1985.
[3] A.N. Norris, Dynamic Green's functions in anisotropic piezoelectric, thermoelastic and poroelastic solids, Proceedings of Royal Society of London A 447 (1994) 175–188.
[4] C.Y. Wang, J.D. Achenbach, Elastodynamic fundamental solutions for anisotropic solids, Geophysical Journal International 118 (1994) 384–392.
[5] D. Nardini, C.A. Brebbia, A new approach to free vibration analysis using boundary elements, in: C.A. Brebbia (Ed.), Boundary Element Methods in Engineering, Springer, Berlin, 1982, pp. 312–326.
[6] N. Kamiya, E. Andoh, K. Nogae, Eigenvalue analysis by the boundary element method, Engineering Analysis with Boundary Elements 12 (1993) 151–162.
[7] C.Y. Wang, J.D. Achenbach, Three-dimensional time-harmonic elastodynamic Green's functions for anisotropic solids, Proceedings of Royal Society of London A 449 (1995) 441–458.
[8] M. Denda, Mixed mode I, II and III analysis of multiple cracks in plane anisotropic solids by the BEM: a dislocation and point force approach, Engineering Analysis with Boundary Elements 25 (2001) 267–278.
[9] C.Y. Wang, 2-D elastostatic Green's functions for general anisotropic solids and generalization of Stroh's formalism, International Journal of Solids and Structures 31 (1994) 2591–2597.
[10] C.Y. Wang, J.D. Achenbach, H. Hirose, Two-dimensional time domain BEM for scattering of elastic waves in solids of general anisotropy, International Journal of Solids and Structures 33 (1996) 3843–3864.
[11] M. Denda, A dislocation and point force approach to the boundary element method for mixed mode crack analysis of plane anisotropic solids, Journal of Chinese Institute of Engineers 22 (1999) 677–693.
[12] C.B. Moler, G.W. Stewart, An algorithm for generalized matrix eigenvalue problems, SIAM Journal of Numerical Analysis 10 (1973) 241–256.
[13] N. Kamiya, S.T. Wu, Generalized eigenvalue formulation of the Helmholtz equation by the Treffts method, Engineering Computations 11 (1994) 177–186.
[14] J.T. Chen, F.C. Wong, Dual formulation of multiple reciprocity method for the acoustic mode of a cavity with a thin partition, Journal of Sound and Vibration 217 (1998) 75–95.